THERMODYNAMICS OF FLUIDS IN MESOPOROUS MEDIA

by

Hyeyoung Cho

A dissertation submitted to the faculty of
The University of Utah
in partial fulfillment of the requirements for the degree of

Doctor of Philosophy

Department of Chemical Engineering

The University of Utah

December 2017

The University of Utah Graduate School

STATEMENT OF DISSERTATION APPROVAL

The dissertation of **Hyeyoung Cho**

has been approved by the following supervisory committee members:

Milind Deo	, Chair	**09/13/2017** Date Approved
John McLennan	, Member	**09/13/2017** Date Approved
Jules Magda	, Member	**09/13/2017** Date Approved
Michael H. Bartl	, Member	Date Approved
Subhash H. Risbud	, Member	Date Approved

and by **Milind Deo** , Chair/Dean of

the Department/College/School of **Chemical Engineering**

and by David B. Kieda, Dean of The Graduate School.

ABSTRACT

Unconventional resources (shale resources) have played a key role in increasing oil production in the past decade in the U.S. The sizes of pores in shales storing the oil are believed to be on the order of nanometers. It is believed that the fluids present in such small nanometer-scale pores have different properties compared to properties measured in the bulk. Fluid bubble points at given temperatures in the nano-sized pores are affected by the influence of pore walls in the vicinity of the fluid molecules. Bubble points affect the proportion of liquid or gas extracted from a given well and, thus, impact the economic viability of oil production. Hence, an accurate measure of a bubble point is important. Most studies on phase behavior of confined fluid systems have focused on modeling pore size dependence upon critical properties with no direct experimental evidence. In this work, direct bubble point measurements of hydrocarbon mixtures in several porous materials are provided. Two different synthesized mesoporous silica materials, SBA-15 and SBA-16, having nano-sized pores of about 4 nm, were used. Mesoporous monoliths with only nano-sized pores and no macro pores were also synthesized using a unique procedure developed in this study. Finally, to see the industrial application of this work, the Niobrara rock which is from one of the famous shale reservoirs in the U.S. was used. These porous materials were characterized well by X-ray diffraction (XRD), nitrogen adsorption/desorption isotherm (BET), transmission electron microscopy (TEM), and scanning electron microscopy (SEM). Binary mixtures of hydrocarbons (decane-methane,

octane-methane) with 90:10 mole ratio were employed. The phase diagrams of those

hydrocarbon mixtures were modeled using a commercial thermodynamic simulator. The

bubble point of bulk (no porous medium) mixtures of decane-methane and octane-

methane, and the bubble point with porous materials (SBA-15, SBA-16, and mesoporous

monoliths) were measured experimentally. Experiments were also performed with

micrometer-sized sand particles and the Niobrara rock. The bubble point results of the

hydrocarbon mixtures in the porous materials and the Niobrara rock were lower than

those in the bulk, while the bubble points with sand were closer to those with bulk

measurements. Differential Scanning Calorimetry (DSC) and Thermogravimetric

Analysis (TGA) results showed that the boiling points of pure decane and decane

saturated in the monolith were different, possibly due to the confinement effect. This

study shows the phase behavior of hydrocarbons in a confined system is different from

that in the bulk system.

TABLE OF CONTENTS

LIST OF TABLES

Tables

LIST OF FIGURES

Figures

ACKNOWLEDGMENTS

Firstly, I would like to thank Professor Milind Deo, a great advisor and a wonderful mentor, for his unlimited support throughout my Ph.D. He encouraged me to think through everything scientifically and logically. Since he has always believed in me, I have learned not to give up when I meet challenges. His enthusiasm, motivation, warm mentoring, and knowledge about science inspired me. I would like to thank my committee members: Professors John McLennan, Jules Magda, Michael Bartl, and Subhash Risbud, for their time, interest, and valuable insights enriching my research. I also would like to thank Department of Chemical Engineering staff who have assisted me and have been good friends: Ribana Milas and Christina Bushman.

My time at the University of Utah was made enjoyable in large part due to all my colleagues and friends. I have been lucky to be in Dr. Deo's research group meeting fabulous colleagues: Palash Panja, Raul Velasco Guachalla, Hyukmin Kwon, Manas Pathak, Thang Tran, Camilo Corredor, Yichen Wang, Ning Bi, and Khalid Rashid and special thanks to Luanjing Guo and Wattana Chaisoontornyotin for being precious friends.

I would like to thank my family for all their love and encouragement; my parents, Sungbae Cho and Sunhee Ahn, who raised me with a love, encouragement, trust, and supported me in all my pursuits; my younger sister, Haejin Cho, who has always been there for me. Lastly, I would like to thank Sangho Kim for his caring and faithful support.

CHAPTER 1

INTRODUCTION

It is hard to imagine industrial operations or even private activities without oil and gas. Not only do they supply energy for heat and power, hydrocarbons are also found in everyday items such as medicines, plastics, and clothing. Furthermore, the International Energy Agency (IEA) reported that the world total primary energy consumption has increased from 4672 Mtoe (5.43e7 kwh) in 1973 to 9425 Mtoe (1.1e8 kwh) in 2014.[1] Oil and natural gas were formed from the remains of prehistoric plants and animals which settled into the seas and large inland lakes along with sand and clay. Over millions of years, the remains were buried deeper and deeper, and the enormous heat and pressure turned them into oil and gas.[2] Historically, oil and gas are obtained from the petroleum reservoirs which are comprised of porous and permeable rocks. The reservoir rock holds significant amounts of oil and gas within the pore spaces.

Conventional hydrocarbon reservoirs have high permeability (0.0001-0.1 mD) and porosity (15-40%), making it easy to develop them using vertical wells. However, as conventional resources are being depleted, unconventional resources are now becoming the focus of new oil and gas exploration and development. These unconventional reservoirs are also called shale reservoirs because of the kind of rock of which they are commonly composed. These shale reservoirs have lower permeability (100 nD-10,000

nD) and porosity (2-7%), and source rocks that contain hydrocarbons can be found there.[3,4] Technological breakthroughs in horizontal drilling and hydraulic fracturing have contributed to developers' ability to extract oil and gas from these unconventional reservoirs. According to the U.S. Energy Information Administration (EIA), of the total U.S. crude oil production in 2017, roughly 50% or about 4.5 million barrels per day of crude oil were produced directly from shale and other tight rock resources.[5] Figure 1.1 shows the total production from tight oil (mostly shale oil) in the U.S. While shale resources and production are found throughout the U.S., the seven most prolific areas are located in the lower 48 states for now. These seven regions accounted for 92% of domestic oil production growth during 2011-2014.[6] As shown in Figure 1.2, they are Bakken, Niobrara, Permian, Eagle Ford, Haynesville, Utica, and Marcellus.

In reservoir engineering, phase behavior of fluids is important because it is a function of the pressure and temperature, and is used to estimate and evaluate the economic feasibility of oil and gas production. The phase behavior of fluids in reservoirs is important during production, separation, and transport of oil and gas.[7] Among the many characteristics of a particular phase behavior, this study focuses on the bubble point of a reservoir fluid.

Oil is produced by creating a pressure difference between the reservoir and the well. Reservoir pressure cannot be readily controlled; however, wellbore pressure can be changed during production. The location of the wellbore pressure on phase diagram of the reservoir mixture is important to extracting oil economically. If the reservoir pressure is below the bubble point of the oil-gas mixture in the reservoir, gas will come out of the mixture. Gas has much lower viscosity and much higher mobility, so it will start

dominating the flow paths and production, and the oil will be left in the reservoir. However, keeping the wellbore pressure higher than the bubble point is usually not economical. From Darcy's law, when the pressure difference between the reservoir and the wellbore is small, the flow rate decreases. Then, the amount of oil produced is small. These two scenarios demonstrate when oil production is not economical. Hence, wellbore pressure ought to be high enough for lowering gas production, but low enough to realize adequate oil rate. The bubble points of reservoir fluids are important properties that determine the relative amounts of fluids produced, and ultimately the economic viability of wells and projects. Moreover, bubble point affects PVT (pressure-volume-temperature) parameters which are important to all facets of reservoirs. PVT parameters, which are oil formation volume factor, solution gas oil ratio, and gas formation volume factor, will change depending on the bubble point.[4]

There is a hypothesis that nano-sized pores that characterize shales might cause the hydrocarbons in the reservoirs to have different thermodynamic properties, including the bubble point, compared to conventional reservoirs.[8–11] Some researchers expected dynamic phase behavior in a confined system is because of the great influence of nano-sized pore walls on the fluids molecules.[3,10–16] There are three strong hypotheses for this phenomenon involving 1) critical point change, 2) capillary pressure change, and 3) molecular adsorption. Zarragoicoechea et al. derived the equation for the critical point shift of a confined fluid from the internal energy and the Van del Waals equation.[17,18] Firincioglu et al. found that the change of capillary pressure in a confined system makes the bubble point change.[8] Third, Dong et al. in 2016 reported simulation results which showed the effects of capillary pressure and adsorption on the phase behavior of confined

hydrocarbon mixtures.[19] Since the interaction between the pore wall and the molecules becomes stronger when the molecules are in a confined system, they can easily be adsorbed by the pore wall. This affects the capillary pressure, and hence the bubble point.

To confirm this phenomenon, many researchers have studied the phase behavior of hydrocarbons in a confined system using simulations. However, there have been only a few experimental studies thus far because of the difficulty of measuring the fluid properties in a confined system.[8,14,19–24] In this research, direct measurements of the bubble point for a hydrocarbon mixture of two components were undertaken in a confined system. In Chapter 2, two different mesoporous materials having similar pore sizes were used to see the effect of porosity and pore morphology, including pore shape, size, and structure, on a hydrocarbon mixture phase behavior. In Chapter 3, mesoporous monoliths were synthesized following a unique method to measure the bubble point of a hydrocarbon mixture in only nano-sized pores (excluding macro pores). Finally, in Chapter 4, to see the industrial application of this work, the bubble point of a hydrocarbon mixture was measured in a Niobrara rock sample, from one of the most productive shale reservoirs in the U.S. Overall, differences and similarities in bubble points in several porous materials and in the bulk are reported.

In the industry, bubble points of hydrocarbons have been measured in a PVT cell using a standard method.[21] The effect of oil confinement is not considered in the measurement because it is negligible in conventional reservoirs due to their high porosity. However, the current standard does not take the effect of confinement into account because it is negligible in conventional reservoirs. The results of this research show the confinement effect on bubble points in low permeability formations. Therefore, it is

necessary to consider the confinement effect. This research provides insight into how

fluids behave in confined systems, which will improve estimations of the thermodynamic

properties of shale reservoirs. This study is an important step toward developing a

measurement standard for shale.

Figure 1.1 EIA official tight oil production data through May 2017.
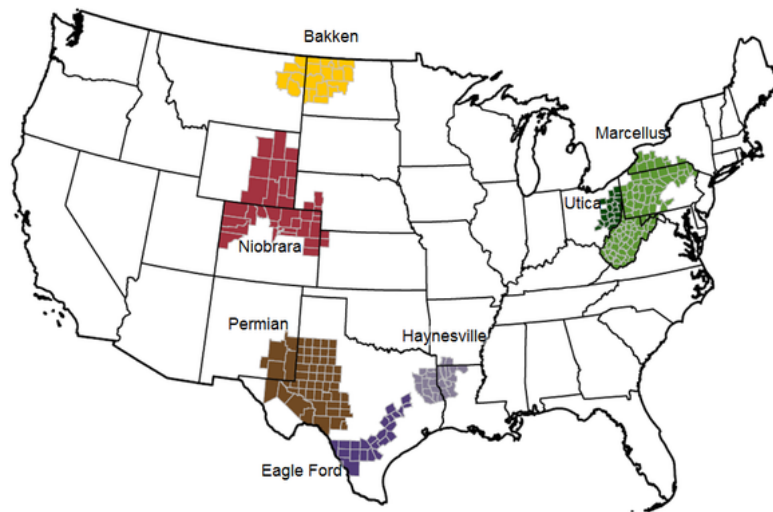
Figure 1.2 EIA official map of U.S. most prominent unconventional plays.

CHAPTER 2

BUBBLE POINT MEASUREMENTS OF HYDROCARBON MIXTURES

IN MESOPOROUS MEDIA

2.1 Introduction

In reservoir engineering, fluid properties are required – as a function of pressure

and temperature – to estimate and evaluate oil and gas production performance and for

the effective management of oil and gas reservoirs. The reason is that as oil and gas are

produced, reservoir pressure decreases and the remaining hydrocarbon mixtures change

in composition, volumetric properties, and phase behavior.[7] The phase behavior of fluids

at reservoir conditions and at different pressures and temperatures is important during

production, separation, and transport of oil and gas.[7] Phase behavior of hydrocarbons and,

specifically, bubble points are measured in pressure-volume-temperature (PVT) cells.

For conventional reservoirs, where the pore sizes are typically of the order of microns,

these bulk measurements are adequately accurate. Equation of State calculations may also

be used for calculating phase compositions, properties and bubble points.[21,25]

Unconventional resources (shale reservoirs) are now becoming the focus of new

oil and gas exploration and development because of technological breakthroughs in

horizontal drilling and hydraulic fracturing.[26] These shale reservoirs have lower

permeability (100 nD – 10,000 nD) and porosity (about 2-7%), and they may be the source rocks that contain hydrocarbons.[3,26] These reservoirs are still in primary production which means that they are produced by creating a pressure difference between the reservoir and the well (or the faces of hydraulic fractures). A pressure gradient is established in the reservoir between the initial reservoir pressure and the wellbore pressure. If the wellbore pressure is below the initial bubble point of the oil-gas mixture in the reservoir, the bubble point of the mixture lies on the pressure trajectory thus established. This pressure trajectory gradually moves away from the wellbore. In the region of the reservoir below the bubble point, gas will come out of solution. Gas has much lower viscosity, and thus much higher mobility, and will start dominating the flow paths and production. Thus, the bubble points of the reservoir fluids are important properties that determine the relative amounts of fluids produced, and ultimately the economic viability of wells and projects.

Typical pore sizes in these rocks may be of the order of 10 nm. Loucks et al. (2009) reported that siliceous mudstone samples from the Mississippian Barnett Shale of the Fort Worth basin, Texas, one of the well-known shales, show that the pores in these rocks are mainly in the nanometer scale.[27] In particular, their scanning electron microscopy images show that the pores are as small as 5 nm. The effect of fluid confinement in these very small pores is not considered in conventional reservoirs with large average pore sizes.[8] Tighter shale reservoirs with lower porosities, permeabilities and average pore sizes in nano meters may present different thermodynamic properties, including bubble point pressures, compared to conventional reservoirs.[9,10] Since traditional phase behavior calculation does not include a confinement effect, there has

been a question if phase behavior calculations would correctly represent the behavior of hydrocarbon mixtures in porous reservoir rocks.[8,11,12] It is important to understand if the phase behavior of hydrocarbons is going to be altered in confined environments.

Research is ongoing to investigate the effect of small pores and confinement on hydrocarbon phase behavior. Two different hypotheses have been proposed. One is that the nearness of the fluid to the nano-sized walls shifts the phase behavior of the confined fluid.[3,10,14,28] Sigmund et al. (1973) reported that when liquid and vapor coexist in a porous medium, the interface between them is curved, and the curvature affects the phase behavior.[21] Pitakbunkate et al. (2015) argued the reason for the different phase behavior in a confined system was related to the orientation and distribution of molecules. They used the Grand Canonical Monte Carlo simulations to quantify this difference.[28] The other theory for having a different phase behavior in a confined system is the change in capillary pressure in a confined system. It has been reported that when the pore size becomes very small, the capillary pressure between the wetting phase and the nonwetting phase becomes significantly larger than in a bulk system and thus affects phase behavior.[8,11,12,15,26] Recently, Dong et al. (2016) reported simulation results for fluid behavior from two factors, capillary pressure and surface adsorption effects.[19] Their study contributes to the emerging theory that more than one factor affects the phase behavior of fluids in nano-sized porous media. Even so, there are no definitive studies on the quantification of each of the factors that may change phase behavior in shales with representative pores of the order of a few nanometers.

There are few experimental studies so far because of the difficulty of measuring the fluid properties in a confined system.[8,14,19,21,22] Sigmund et al. (1973) reported the

effect of porous media on the phase behavior of hydrocarbon binaries.[21] Glass or steel spheres were used as porous media, and they were packed in the designed PVT cells to measure dew-point pressures of fluids. In their research, the differences in dew-point pressure between a packed and unpacked PVT cell were within the limits of experimental error. However, the published results of condensation by Buzinov et al. (1976) were different.[23] They observed vapor pressure suppression for pure hydrocarbons – ethane, propane, isobutene, and butane – in porous media with particles of sizes in the100-200 micron range. It may be possible to observe changes in phase equilibrium in a sufficiently fine porous medium less than a micron in size, since the glass or steel spheres were much bigger than micron size. Luo et al. (2016) presented experimental results on the bubble points of octane and decane confined in controlled pore glasses with pore sizes of 4.3 nm and 38.1 nm using DSC (Differential Scanning Calorimetry) thermograms.[9] The results indicated that bubble-points were affected by pore diameter. The effect of the confined system having 38.1 nm pore size was negligible, and bubble point shift was as large as $\pm$ 15 K in the system with 4.3 nm of pore size. Two later publications expanded on these results and provided Differential Scanning Calorimetry (DSC) data for different nanoporous materials and mixtures.[29,30]

The focus of research in flow in nanoporous media has mainly been on the effect of pore size.[14,18,31–33] Most of the studies are models of the effect of confinement on thermodynamic properties. Zarragoicoechea et al. (2004) illustrated the difference in component critical properties between confined and bulk fluids. It has been suggested that the critical properties of the components are functions of the ratio of the molecular size to the pore size.[18] Devegowda et al. (2012) pointed out that interactions between

molecules, and between molecules and the pore surface, are known to alter fluid properties because the pore surface available per unit volume increases as the pore size decreases.[34] Factors other than size, such as surface activity of the material, may also affect phase behavior.

In this work, two different mesoporous materials having similar pore sizes were used to see the effect of pore morphology on hydrocarbon mixture phase behavior. Morphology is the study of form comprising shape, size, and structure.[35] In materials that are characterized by nanometer sized pores, morphology is an important factor since it significantly affects the physical and chemical properties.[36,37] Physisorption phenomenon and the isotherm are driven by the relationship between the amount of the adsorbed molecules and the relative pressure of the molecules, at a specific temperature.[38] Porosity plays an important role in geology as it controls fluid storage, flow, and transport in aquifers, and oil and gas reservoirs.[39] Porosity, the extent and connectivity of the pore structure, as well as the properties of individual minerals and the bulk properties of the rock, are all important in determining the fate of fluids in naturally occurring porous media.[39]

SBA-15 and SBA-16 were chosen for the study and synthesized since these mesoporous materials have high BET surface areas (690 – 1040 m^2/g) and small aligned pores (4.6 – 30 nm).[40] The purpose of synthesizing these mesoporous materials was to create nanomaterials with pore size in the range found in gas- or liquid-bearing shales in the United States. These porous materials were synthesized in our laboratories because large quantities were required for experimentation and the synthesis conditions provided us ways to control material properties. SBA-15 is commonly available, but SBA-16 less

so. SBA-15 and SBA-16 have highly ordered hexagonal and cubic mesoporous silica structures. These were synthesized since large quantities were necessary for experimentation. A sister project was sintering of the synthesized powders into artificial rocks. This would allow creation of calibrated 'artificial rocks' for property measurement and model testing. Maheshwari et al. (2016) were able to amalgamate the powders into robust mesoporous compacts.[41]

The synthesized mesoporous materials were thoroughly characterized (morphology, nitrogen physisorption, porosity, and pore structure). In oil reservoirs, presume that the fluids are drained isothermally by lowering the pressure in the reservoir. Sometime during this process, the mixture crosses the bubble point curve and enters the two-phase region. Two fluid mixtures of decane and methane (90:10 mole ratio) and octane and methane (90:10 mole ratio) were used to represent the reservoir fluid and the depressurization process was carried out. Bubble point pressures of decane-methane mixtures at two different temperatures (38 $^{\circ}$C and 52 $^{\circ}$C) and octane-methane mixture at one temperature (38 $^{\circ}$C) were measured inside these porous media. Differences and similarities in bubble point pressures in the mesoporous materials and in the bulk are reported.

2.2 Materials and Methods

Silica-based mesoporous materials, SBA-15 and SBA-16, were prepared according to the procedure described in the previous literature.[40] Since the materials were synthesized, a characterization program was undertaken to ensure material quality, and only selected results are reported. N_2 adsorption/desorption isotherms were obtained

using a Sorptometer (Gemini 5, Micromeritics) at 77 K. The specific surface areas of the samples were calculated by the BET method, and pore size distributions were calculated by the BHJ method. Pore images of mesoporous materials were examined by transmission electron microscopy (FEI Tecnai 12 Transmission Electron Microscope).

The plan was to measure bubble point pressures of decane-methane mixtures and octane-methane mixtures at a given temperature. In order to understand the range of these bubble point pressures, well-established thermodynamic models were first used to calculate the bubble point pressures. The phase diagram of the binary mixture of decane and methane with 90:10 mole ratio and the phase diagram of octane and methane mixture with 90:10 mole ratio were modeled with the commercial thermodynamic simulator, Winprop. Winprop is a product of Computer Modeling Group (CMG). Peng-Robinson (1976) equation of state was applied. Peng-Robinson equation of state is generally known to be superior in predicting phase compositions and liquid densities of many hydrocarbon mixtures. Bubble points were measured at 38 ^{o}C (100 ^{o}F) and 52 ^{o}C (125 ^{o}F) for 90:10 molar mixtures of decane and methane. The thermodynamic calculations using the Peng-Robinson equation of state predict these bubble points to be 2620 kPa and 2896 kPa, respectively. Also, bubble points of octane and methane with 90:10 mole ratio were measured at 38 ^{o}C (100 ^{o}F). The predicted bubble points of these mixtures calculated by thermodynamic calculations using the Peng-Robinson equation of state are 2537 kPa.

Bubble point pressure measurements were performed using a customized apparatus built in-house (see Figure 2.1). A 16 cm long stainless steel tube with 0.95 cm outer diameter and 0.08 cm wall thickness was connected to two high-pressure syringe pumps (ISCO pumps) for decane (or octane) and water, and two gas cylinders of methane

and nitrogen, and a vacuum pump. This system was placed in an oven. A data acquisition

system permitted recording of pressure in the system and volume on a continuous basis.

Decane (or octane) is first charged into the system followed by methane in an amount

that would bring the mole ratio of methane to 10% in the mixture. Methane is bubbled

through decane to increase contact area and equilibration. The temperature of the oven

was raised to 38 ^{o}C (100 ^{o}F) or 52 ^{o}C (125 ^{o}F). After the temperature in the oven was

steady and no longer fluctuating, the pressure of the system was raised by injecting water

continuously to the system at a rate of 0.1 mL/min. The water was used only for

pressurizing the system. The effect of water on phase behavior at this temperature was

assumed not to affect the hydrocarbon phase behavior. The solubility of methane in

decane is about 2000 times larger than the solubility of methane in water.[42,43] The

mesoporous materials used were hydrophobic.[44] Once the pressure reached 8274 kPa

(1200 psi), the pressure of the system was decreased by withdrawing water at a rate of 0.1

mL/min to ensure that equilibrium was attained during the depressurization process.

Pressure and volume are continuously recorded. When gas first appears in the system,

every incremental pressure change will be associated with a relatively larger level of

volumetric change. The pressure-volume plot may be used to deduce bubble point

pressure. A regression technique was used in MATLAB to monitor the change in slope

continuously and a bubble point pressure was determined. An identical procedure was

used for experiments where no porous material was packed inside the tube (bulk

measurement), and experiments where SBA-15, SBA-16, or silicon dioxide (sand) was

packed inside the pressure tube.

2.3 Results and Discussion

Characteristics of SBA-15 and SBA-16 are widely available, and hence are not discussed in this paper in detail. Since the materials were synthesized, however, selected results are shown to establish the quality of the materials. The pore size distributions of the two materials are also shown in Figure 2.2(a) and (b). Both the pore size distribution curves have one sharp peak around 4 nm, and the pore size range of the synthesized SBA-16 is slightly narrower than the one of SBA-15. Thus, mesoporous pore size did not affect bubble point measurements.

Figures 2.2(c) and (d) show the TEM images of the synthesized SBA-15 and SBA-16. They both have highly ordered small pores. As shown in Figure 2.2(c), the synthesized SBA-15 has a two-dimensional mesoporous structure. On the other hand, the synthesized SBA-16 has a three-dimensional mesoporous structure (see Figure 2.2(d)). In these TEM images of the synthesized SBA-15 and SBA-16 (see Figure 2.2(c) and (d)), the distance between the mesopores was estimated to be less than 5 nm, which was in good agreement with the d-spacing calculated from the XRD data (not shown here). These images of pore structures are consistent with previous observations.[19,45–48] Gubbins et al. (2014) showed that a slit-shaped pore is easier to treat from a modeling perspective since the confinement was only in one direction. Curved pore walls lead to confinement in two or three dimensions and stronger steric hindrance by the wall.[22]

Figures 2.2(e) and (f) show the nitrogen adsorption/desorption isotherms of SBA-15 and SBA-16. These measurements showed hystereses at relative pressure ranges of about 0.4 to 0.7. The relative pressure range of hysteresis for SBA-15 is 0.4 to 0.6 and 0.45 to 0.65 for SBA-16. The average pore size of the synthesized mesoporous materials

was calculated by the BJH method based on N_2 adsorption/desorption isotherms data. The calculated average pore size of the synthesized SBA-15 was 3.5 nm and the one of the synthesized SBA-16 was 3.7 nm. These values match well with the pore size distribution curves in Figures 2.2(a) and (b). The synthesized SBA-15 has 16 mmol/g of adsorbed nitrogen amount, and SBA-16 has 15 mmol/g. SBA-15 has a BET surface area of 752 m^2/g with 0.44 cm^3/g of pore volume, while SBA-16 has a BET surface area of 699 m^2/g with 0.39 cm^3/g of pore volume. All surface and pore size characteristics of the synthesized SBA-15 and SBA-16 are listed in Table 2.1.

Formation of bubbles under confinement is expected to affect bubble point pressures of confined mixtures.[49] Porosities of the synthesized SBA-15 and SBA-16 were calculated, and are reported in Table 2.1. The micro pore volume was measured by t-plot from BET measurements. This is the volume from the pores having less than 2 nm of pore size. The meso pore volume was calculated by subtracting the micro pore volume from the total pore volume from BET method as well. The synthesized SBA-15 has 0.11 cm^3/g micro pore volume and 0.33 cm^3/g meso pore volume. The synthesized SBA-16 has 0.09 cm^3/g micro pore volume and 0.3 cm^3/g meso pore volume. Total porosity was determined by adding macro porosity and the inner porosity. As shown in Table 2.1, the total pore volume of the synthesized SBA-15 is 0.44 cm^3/g and for the synthesized SBA-16 is 0.39 cm^3/g. The calculated inner porosities of SBA-15 and SBA-16 were 22% and 14%, respectively. The macro porosity was calculated using properties of silicon dioxide grains of particle size distribution similar to SBA-15 and SBA-16. The particle sizes of silicon dioxide ranged from 0.5 to 10 μm, with approximately 80% of the particles between 1 to 5 μm. The volume of silicon dioxide packed in this system was calculated

from its density (2.6 g/ml). The macro porosity calculated using known total volume was 62%, which is in good agreement with the published relationship between porosity and grain size/shape.[50] From these results, the total porosity of two mesoporous materials was calculated to be 84% for the synthesized SBA-15 and 76% for the synthesized SBA-16.

The phase diagram of the binary mixture of decane and methane with a 90:10 mole ratio modeled with the Winprop module of the CMG reservoir simulator is shown in Figure 2.3. The mixture has a critical temperature of $344^{\circ}C$ and a critical pressure of 3447 kPa. The cricondentherm was $345\,^{\circ}C$ and the cricondenbar was 3697 kPa. The bubble point and the dew point curves are shown in Figure 2.3. The bubble points were measured at temperatures of $38\,^{\circ}C$ and $52\,^{\circ}C$, and the P-T diagram shown in Figure 2.3 was used to estimate the bubble point pressures and help guide the experiments. The bubble point pressure at $38\,^{\circ}C$ is seen to be 2620 kPa and at $52^{\circ}C$ as 2896 kPa (please see Figure 2.3).

The phase diagram of the octane and methane mixture with a 90:10 mole ratio modeled with the Winprop module of the CMG reservoir simulator is shown in Figure 2.4. The critical temperature and pressure of this mixture are $292\,^{\circ}C$ and 3932 kPa, respectively. The cricondentherm and cricondenbar were determined to be $292\,^{\circ}C$ and 4137 kPa, respectively. The bubble point pressure at $38\,^{\circ}C$ is found to be 2537 kPa, slightly lower than the decane-methane mixture of the same molar proportion. These values provided a range of expected bubble point pressures when experiments were performed.

The experimental bubble point pressures were obtained from the pressure-volume relationships inside the porous medium. When there is only liquid in the system, there is

a much sharper change in pressure for any unit volume change. When the first bubbles appear and the system becomes two phases, the pressure change becomes more gradual for any unit volumetric change. This property change is used to identify the bubble point. This technique for bubble point measurement has been employed previously, albeit in high-pressure cells.[51] The pressurizing fluid used in the experiment was water. The water-hydrocarbon interface was inside the porous medium when the transition occurred. All pressure-volume plots were obtained with a slow depressurization process.

Figure 2.5 shows some sample pressure-volume plots of decane-methane mixture at two different temperatures for the bulk measurement (no porous medium). A regression code in MATLAB was used to fit a line to the lower portion of the graph and a separate line to the upper curve. The intersection of these two lines produced the bubble point pressure. The regression coefficient for the entire data set was over 0.98 (R^2=0.98) in all of the fitted lines. The bubble point pressures obtained using this technique are reported in Table 2.2. For the mixture chosen, the bubble point pressures were 2546 kPa at 38 ^{o}C and 2720 kPa at 52 ^{o}C (average values). The experimentally measured bubble points increased with temperature and were in reasonably close agreement with the values provided by thermodynamic calculations.

The bubble point measurements were performed with pressure tubes packed with mesoporous materials. All experimentally measured pressure-volume plots with the synthesized SBA-15 and SBA-16 (shown in Figure 2.6) have the same shape as the graph of the bulk measurements. Once again, the bubble point pressures were determined by fitting the lower and the upper portions of the curves and finding intersections.

To see the effect of nano-sized pores on bubble point pressure, the bubble point

pressures were also measured with silicon dioxide (SiO_2) powders. The SiO_2 (Sigma-Aldrich) consisted of 0.5 to 10 μm of particles (with approximately 80% between 1 to 5 μm). It should be noted that the particle sizes of SBA-15 were 1-2 μm and those of SBA-16 were in the 2-5 μm range. Thus, SiO_2 created a similar pore system, but without the presence of nanopores that characterized SBA-15 and SBA-16. In Figure 2.7, the experimentally measured P-V plots with the silicon dioxide are shown. The interpreted bubble points as shown in Table 2.2 are closer to the bulk than to the bubble points measured with SBA-15 and SBA-16 as porous media. The measured bubble points for all media increased with temperature as expected.

Table 2.2 provides a summary of all bubble point measurements for the decane-methane system. Most of the experiments were repeated and the multiple sets are shown in Table 2.2. Standard deviations are shown in Table 2.2. The average bubble point pressures (when multiple experiments were performed) with the synthesized SBA-15 are 1690 kPa at 38 ^{o}C and 2186 kPa at 52 ^{o}C. The bubble point pressures in SBA-16 are higher at 2017 kPa at 38 ^{o}C and 2468 kPa at 52 ^{o}C. The bubble point pressures in SBA-15 and in SBA-16 were lower than in the bulk. The suppression of bubble point is higher in SBA-15 in comparison to SBA-16. This may be due to the higher inner porosity in SBA-15 comprising of nano channels (22% compared to 14% as shown in Table 2.1). The bubble point pressures with SiO_2 at two different temperatures were closer to the simulated and bulk results. The bubble point pressures with SiO_2 are 2503 kPa at 38 ^{o}C and 2689 kPa at 52 ^{o}C. The nano porosity in the mesoporous materials appears to be affecting the bubble points.

Bubble points with error bars are plotted in Figure 2.8. There are some variations

in the experimental measurements, but overall the variability appears reasonable and acceptable.

Bubble point pressures were measured for a second mixture containing 90 mole% octane and 10 mole% methane. The procedures employed in making these measurements were identical to those described previously. Pressure-volume plot of octane-methane mixture at 38 $^{\circ}$C for when no porous media were present is shown in Figure 2.9. The bubble point measured was close to that predicted by the thermodynamic simulator in two sets of experiments (please see Table 2.3). The pressure-volume plots for the octane-methane mixture with the two mesoporous media are shown in Figure 2.10. The interpreted bubble points were lower than the bulk in both the systems. The porous medium with SBA-15 exhibited lower bubble points than when the tube was packed with SBA-16. All of the results, including repeated experiments, are summarized in Table 2.3.

There has been a discussion regarding suppressed bubble points of oils in shales after the emergence of tight oil shale plays. A number of modeling studies and some experimental investigations have presented evidence that the thermodynamic properties of mixtures may be altered in confined spaces. The process of oil production from shales is complex, and is affected by multiple factors. Experiments performed in this study mimicked the depressurization process. Experimental evidence gathered on two mixtures suggest that bubble points may indeed be lower in mesoporous media characterized by nano-sized pores than in the bulk. Even though simple mixtures were used, the experiments performed are complex. The system response is over the entire porous medium, and experiments with in-situ monitoring will be necessary to verify and quantify the differences observed and relate them to fundamental pore morphology and phase

change in confined spaces. The lowering of bubble points may be explained using the Kelvin equation. To account for the surface tension forces in pores smaller than a certain diameter, bubble point pressures at isothermal conditions decrease.

2.4 Conclusion

Economic viability of wells producing from low-permeability formations depends on the relative amounts of oil and gas produced from these wells. Bubble point pressures of oils in the formation affect the ratio of oil to gas produced. Bubble point pressures are usually measured in visual pressure cells in a laboratory. These measurements have been adequate for conventional oil and gas reservoirs, where the pore sizes are typically of the order of 5-10 μm. There have been questions about the applicability of these measurements for porous media characterized by pore sizes of the order of nanometers. Specifically, several models have been developed to show that bubble point pressures of hydrocarbon mixtures are affected in confined nano-sized channels. In this work, direct measurements of bubble point pressures for a hydrocarbon mixture of two components were undertaken in mesoporous media with nanometer-sized pores.

Two mesoporous siliceous materials with average pore sizes of about 4 nm (SBA-15 and SBA-16) were synthesized and fully characterized, including inner porosity. BET measurements and TEM images showed the materials to have a uniform nanoporous structure. Bubble point pressures of a mixture of decane and methane (90:10 mole ratios) and octane and methane (90:10 mole ratio) were measured in a pressurized system with and without the presence of the synthesized mesoporous materials. Experiments with decane-methane mixtures were performed at 38 ^{o}C and 52 ^{o}C while experiments with the

octane-methane mixtures were performed at 38 ^{o}C. Bubble points in the bulk (without porous media) were reasonably close to values predicted by a thermodynamic model. Bubble points with micron-sized sand particles (with no nano porous structure) were closer to the bulk measurements. Bubble point transitions inside the mesoporous media occurred below the bubble point pressure values in the bulk used in this study. The bubble points in SBA-15 with an inner porosity of 22% were slightly lower than in SBA-16 with an inner porosity of 14%. These measurements provide evidence that bubble points of oils may be suppressed in mesoporous media.

Table 2.1 Surface and porosity characteristics of the synthesized SBA-15 and SBA-16.

	BET surface area (m²/g)	Average pore size[1] (nm)	Total pore volume (cm³/g)	Micro pore volume[2] (cm³/g)	Meso pore volume[3] (cm³/g)	Total porosity[4] (%)	Inner porosity (%)
SBA-15	752	3.5	0.44	0.11	0.33	84	22
SBA-16	699	3.7	0.39	0.09	0.3	76	14

[1]BJH method, [2]t-plot, [3]Meso pore volume = Total pore volume − Micro pore volume, [4](macro pore volume + inner pore volume)/total volume

Table 2.2 Bubble point pressures of the mixture of 90% decane and 10% methane with mesoporous materials (SBA-15 and SBA-16) and without (bulk). Data on measurements of bubble points of the same mixture with sand particles (SiO_2) are also shown.

Temp. (°C)	Bubble point pressure (kPa)								
	Simulated	Bulk		SD[1]	SiO_2	SBA-15		SD[1]	SBA-16		SD[1]
		Experiments			Experiments	Experiments			Experiments		
38	2620	1st	2579	46	2503	1st	1696	29	1st	2034	18
		2nd	2481			2nd	1731		2nd	1999	
		3rd	2579			3rd	1696				
52	2896	1st	2717	3	2689	1st	2220	35	2468		
		2nd	2723			2nd	2151				

[1]Standard deviation

Table 2.3 Bubble point results with mesoporous materials (SBA-15 and SBA-16) compared to the simulated and bulk experimental for a mixture of 90% octane and 10% methane.

Temp. (°C)	Bubble point pressure (kPa)							
	Simulated	Bulk			SBA-15		SBA-16	
		Experiments	SD[1]		Experiments	SD[1]	Experiments	SD[1]
38	2537	1st	2503	4	1st	1765	86	1st	2186	41
		2nd	2510		2nd	1937		2nd	2268	
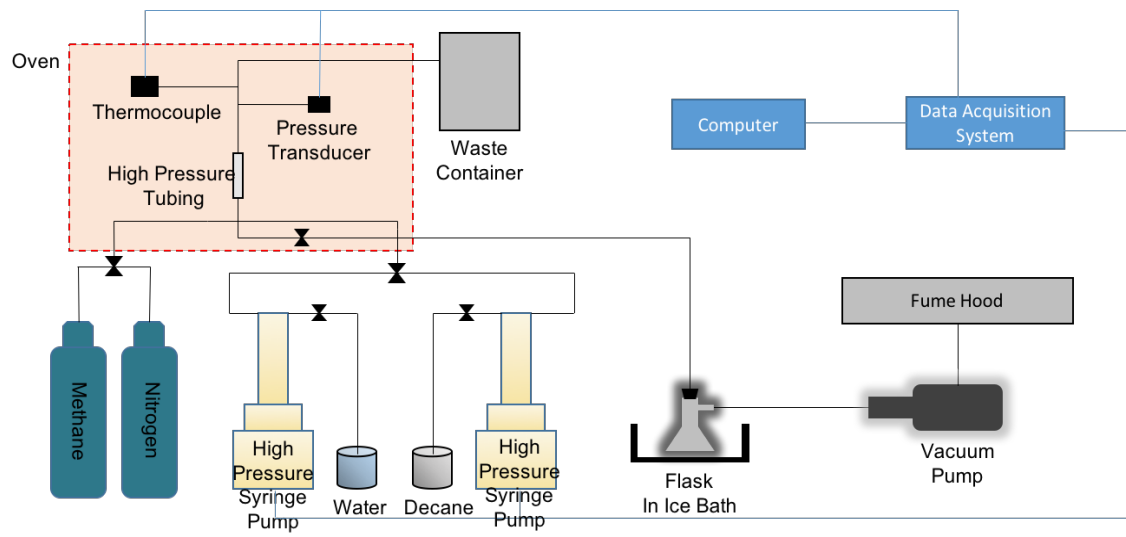
Figure 2.1 Schematic of the experimental system used in measuring bubble points of

hydrocarbon mixtures in porous media.
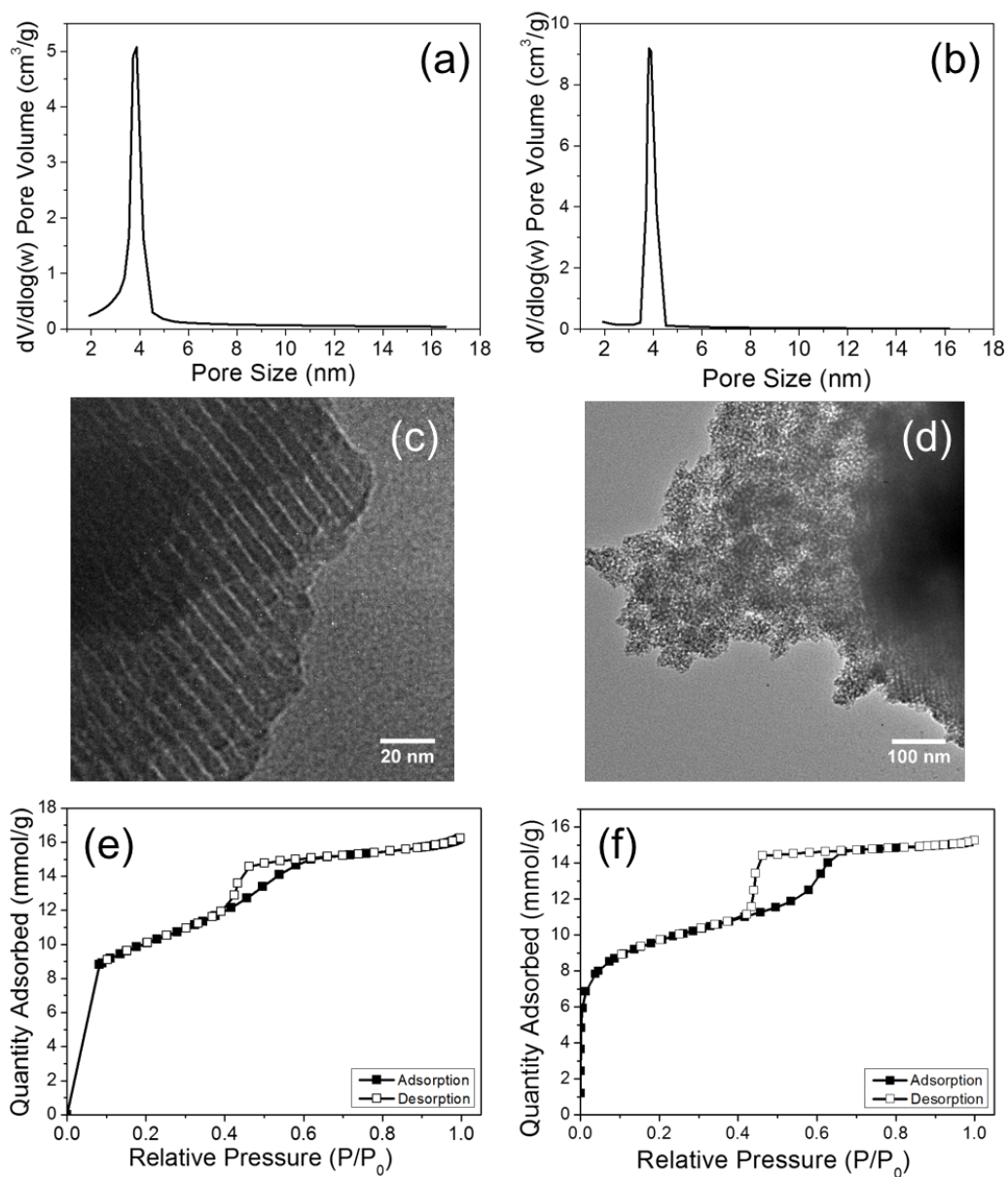
Figure 2.2 Characterization of the synthesized SBA-15 and SBA-16: pore size distribution of SBA-15(a) and SBA-16(b); TEM images of SBA-15(c) and SBA-16(d); N$_2$ adsorption/desorption isotherm of SBA-15(e) and SBA-16(f).
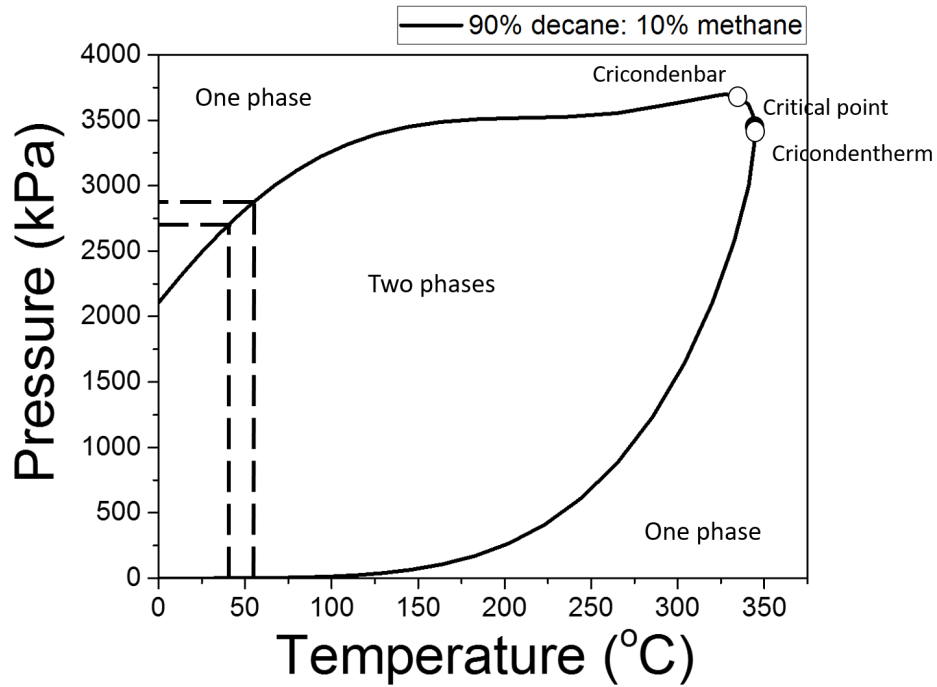
Figure 2.3 Pressure-temperature (PT) plot of a 90% decane and 10% methane molar mixture obtained using a thermodynamic program employing the Peng-Robinson equation of state. The bubble points at 38 ^{o}C and 52 ^{o}C are observed to be 2620 kPa and 2896 kPa, respectively.
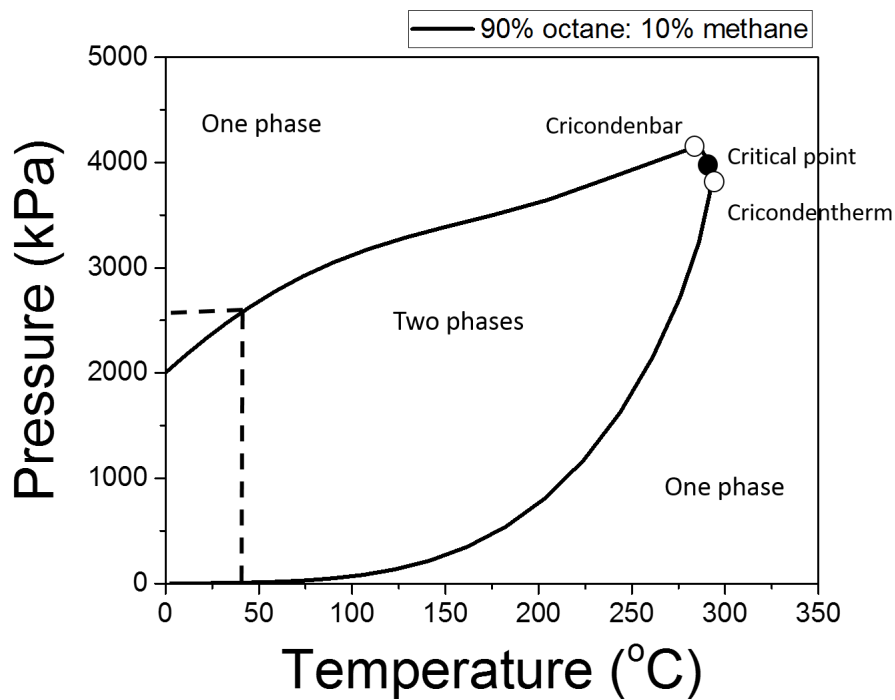
Figure 2.4 Pressure-temperature (PT) plot for a 90% octane and 10% methane molar

mixture obtained using a thermodynamic program employing the Peng-Robinson

equation of state. The bubble points at 38 °C are observed to be 2537 kPa.
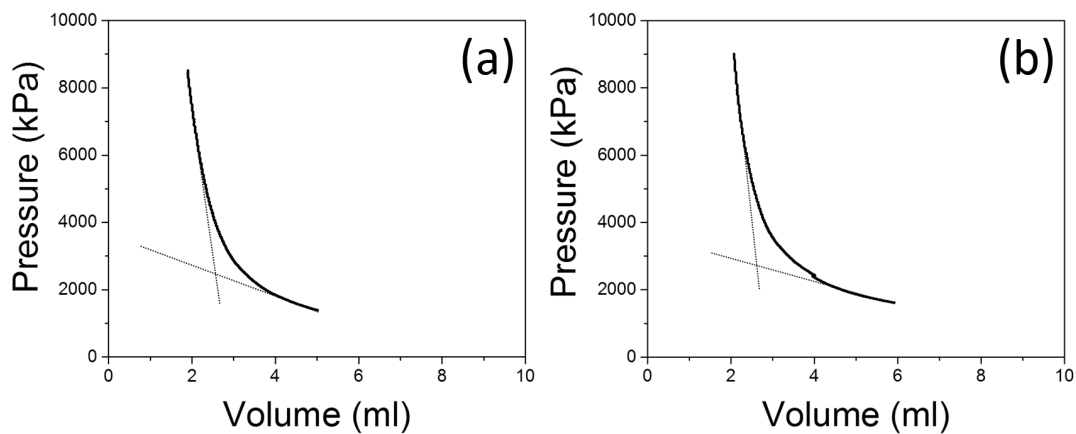
Figure 2.5 Experimentally measured pressure-volume plots for the 90% decane and 10% methane molar mixture at 38 $^{\circ}$C (a) and 52 $^{\circ}$C (b). These measurements were performed without a porous medium in the pressure tube.
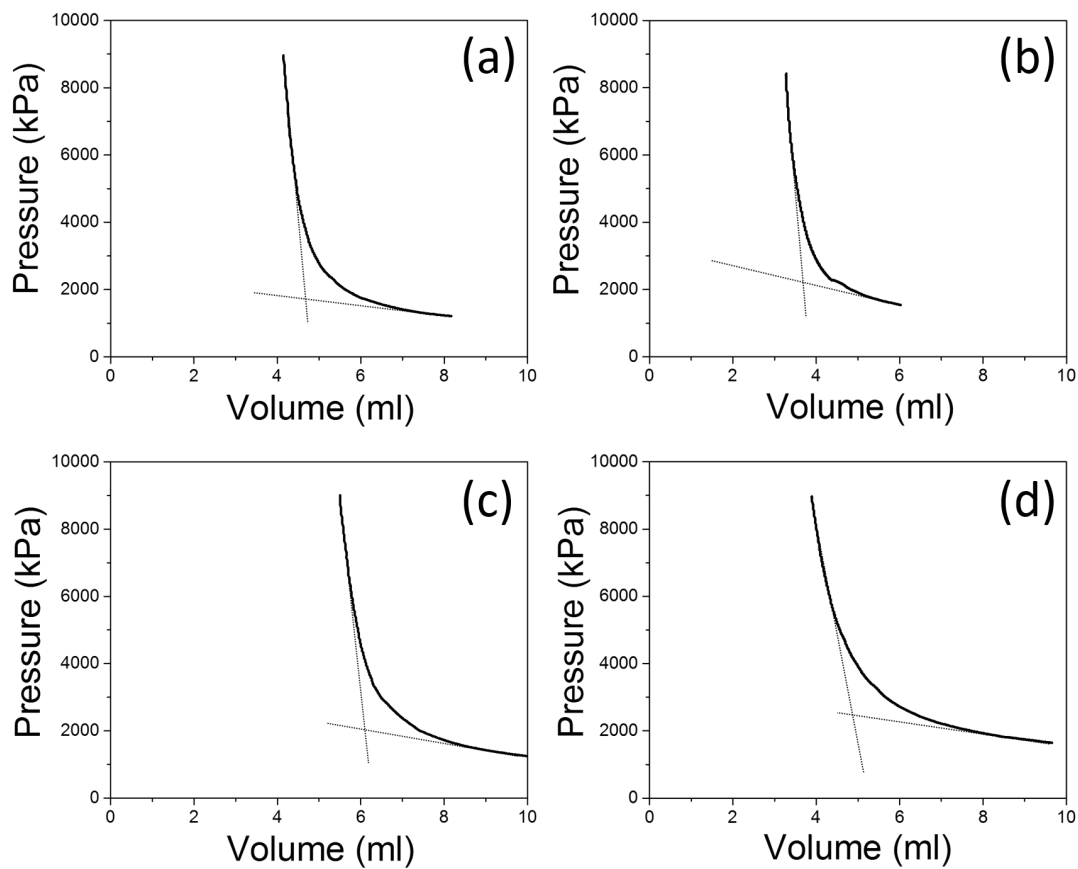
Figure 2.6 Experimentally measured pressure-volume plots for the 90% decane and 10% methane molar mixture. The plots are for SBA-15 at 38 $^{\circ}$C (a), 52 $^{\circ}$C (b) and for synthesized SBA-16 at 38 $^{\circ}$C (c), 52 $^{\circ}$C (d).
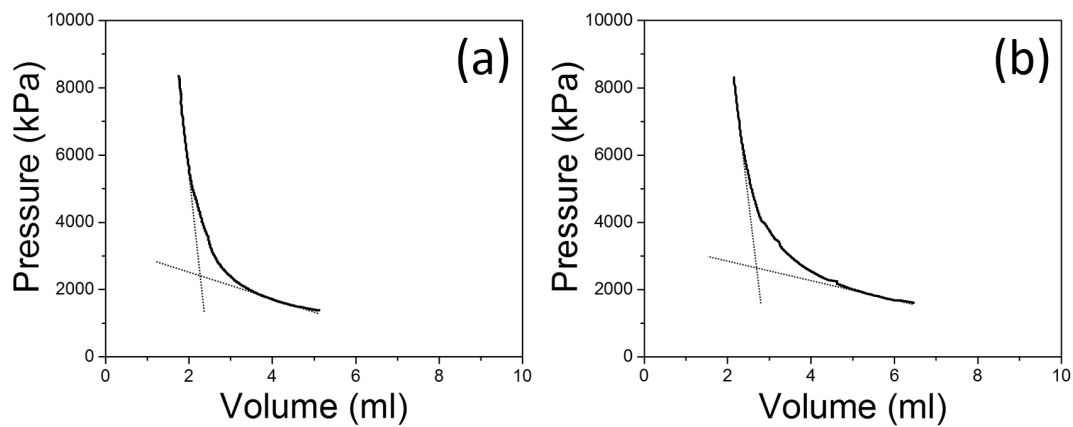
Figure 2.7 Experimentally measured pressure-volume plots for the 90% decane and 10% methane molar mixture. The plots are for SiO_2 at 38 ^{o}C (a) and 52 ^{o}C (b).
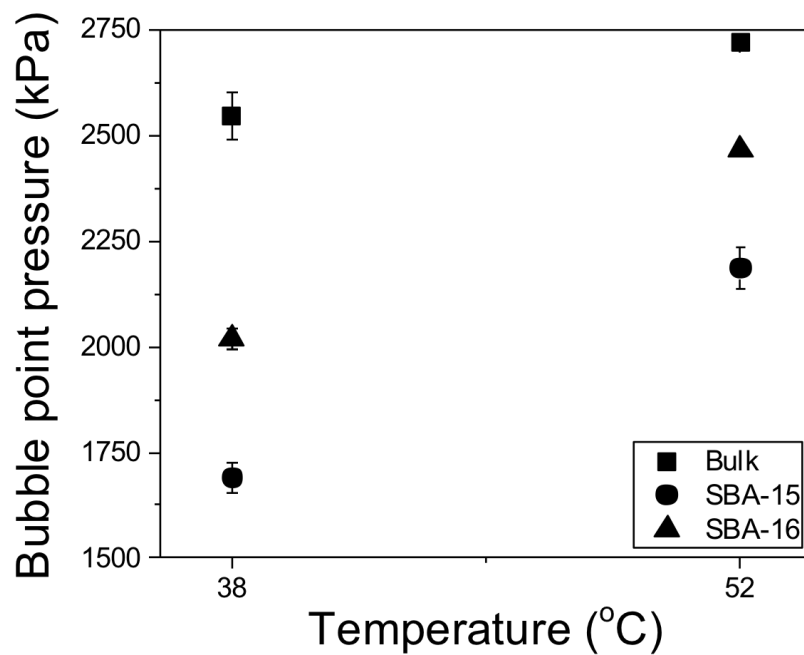
Figure 2.8 Combined results of the experimentally measured bubble point pressures of

90% decane and 10% methane molar mixture in the bulk (no porous medium) and with

SBA-15 and SBA-16 at 38 ^{o}C and 52 ^{o}C. Error bars are shown in the figure.
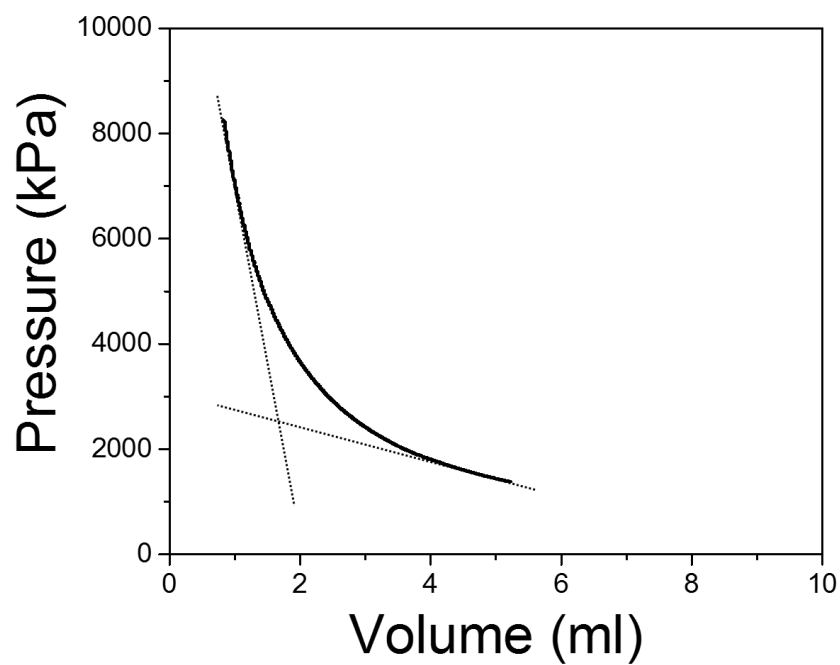
Figure 2.9 Experimentally measured pressure-volume plots for the 90% octane and 10% methane molar mixture at 38 ^{o}C. These measurements were performed without a porous medium in the pressure tube.
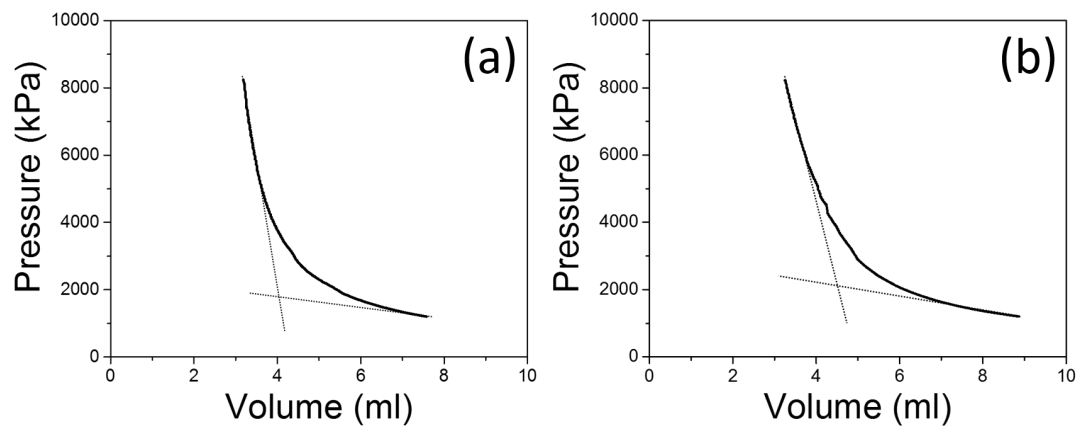
Figure 2.10 Experimentally measured pressure-volume plots for the 90% octane and 10% methane molar mixture. The plot is for SBA-15 at 38 $^{\circ}$C (a) and for SBA-16 at 38 $^{\circ}$C (b).

CHAPTER 3

MEASUREMENTS OF HYDROCARBON BUBBLE POINTS IN SYNTHESIZED

MESOPOROUS SILICEOUS MONOLITHS

3.1 Introduction

Shale reservoirs are the focus of new oil and gas exploration and development.

This growth is aided by technological breakthroughs in horizontal drilling and hydraulic

fracturing.[3] These shale reservoirs have lower permeability and porosity, with pore size

distributions ranging between 1 – 20 nanometers (nm). Unlike conventional reservoirs,

they can be the source rocks that contain hydrocarbons.[3,8] During production, fluids are

depressurized, isothermally in reservoirs. This fluid expansion followed by bubble point

transition with gas evolution takes place inside the nanometer-sized pores. Fluid

confinement in these pores may affect important thermodynamic fluid characteristics.

The phase behavior of reservoir fluids is essential in reserve evaluation, well performance

prediction, reservoir management, and enhanced oil recovery.

It is well known that shales have a complex mineralogy characterized by the

presence of clays and organic matter in various amounts.[52] Loucks et al. (2009) showed

that siliceous mudstone samples from the Mississippian Barnett Shale of the Fort Worth

basin in Texas (based on scanning electron microscopy images) consisted of pore sizes of

about 5 nm.[27] Fluid phase behavior in confined materials has been the subject of many

studies. It has been observed that a fluid's phase envelope shifts, and hence the critical properties change under confinement.[3,10,28] Many of the researchers who studied this fluid behavior under confinement performed their research theoretically.[8,10–12,26,28,53] For example, Behanz et al. (2013) used a Monte Carlo simulation to demonstrate the effect on a temperature-density phase diagram as a decrease in critical temperature after a certain minimum pore size has been reached.[10] Also, Pitakbunkate et al. (2015) used Grand Canonical Monte Carlo simulations to comprehend the reason for the change in interaction as being due to the different orientation and distribution of molecules.[28] Recently, Dong et al. (2016) reported simulation results for fluid behaviors from both capillary pressures and adsorption effects.[19] Different previous studies show that thermodynamic properties of fluids under confinement deviate from their bulk value; however, there are few experimental studies so far.[9,15,21,23]

In one of the few existing experimental studies, Sigmund et al. (1973) reported the effect of porous media on the phase behavior of hydrocarbon binaries (methane-butane and methane-pentane).[21] They designed a PVT cell that was packed with glass or steel spheres as porous media. From their study of the effect of curvature on dewpoint pressures, they found that any differences in behavior between packed and unpacked PVT cells were within the limits of experimental error. They hypothesized that the effect of curvature on equilibrium pressure will not be of practical significance until the particle size approaches the clay-size range (less than 1 micron radius). Luo et al. (2016) found specific pore sizes affecting phase behavior. They presented experimental results on the bubble points of octane and decane confined in controlled-pore glasses with pore sizes of 4.3 and 38.1 nm using differential scanning calorimetry thermograms.[9] They found that

the bubble point is dramatically affected by pore diameter: the bubble point shift of confined hydrocarbon is negligible at 38.1 nm, and the bubble point shift is as great as ± 15 K at 4.3 nm. Recently, additional DSC data of boiling points of hydrocarbons in different mesoporous materials were published.[29,30] Direct measurement of bubble points of hydrocarbon mixtures in mesoporous materials were reported earlier in Chapter 2.[20] These results show that the bubble points may be lower in nano-sized porous media. There has been no published research focusing on the relationship between exclusively nano-sized pores and saturation pressure. To accomplish these measurements, materials with only nano-sized pores must first be synthesized.

Silica-based mesoporous materials having the same pore size range as typical shales were chosen to understand the phase behavior of hydrocarbons in shales. Ordered mesoporous materials have attracted much attention as adsorbents, catalysts, and catalyst supports because of their high surface area and large pore volume with narrow pore size distribution.[45,54] One of the most investigated materials among ordered mesoporous materials is SBA-15 which has highly ordered hexagonal mesoporous silica structures. However, packing SBA-15 into a tube for saturation pressure measurements creates macro-porosity between particles. It is desirable to eliminate this macro-porosity to get an understanding of the effect of nano-sized pores alone on saturation pressures. To evaluate the effect of only the nano-sized pores on the thermodynamic properties, the silica-based mesoporous monoliths were synthesized using the same reactants used in the synthesis of SBA-15. These monoliths can be synthesized into desired shapes by putting them into customized containers. Since these monoliths only have intragranular pores, not intergranular pores, the effect of the nano-sized pores on the saturation pressure was

separated. The mesoporous monoliths can be promising substrates for macromolecular separations because of their lack of external surface area.[55,56]

There has been a challenge to synthesize crack-free monoliths. Cracks form in the process of creating monoliths, making them unsuitable for use as media for saturation pressure measurements. A couple of techniques have been proposed for the creation of crack-free monoliths, only with partial success. For example, in the super critical CO_2 drying, which is one of the methods, the stage of diffusion CO_2 inside the gel is difficult to control, and the processing period is too long, which limits the practical application for monolithic mesostructured silica.[57–59] Yang et al. (2003) reported a rapid method for preparing crack-free mesostructured silica monoliths using liquid paraffin.[60] When poured onto the silica gel to conduct thermal treatment, the liquid paraffin seeps into the interface between the monoliths and the container when the monoliths shrink, thus avoiding exposing the gel to the atmosphere. However, the liquid paraffin is difficult to remove completely after the monoliths have been synthesized.

In this work, the crack-free monoliths were synthesized by controlling the evaporation rate and the monoliths were used to find the effect of a confined system on saturation pressure. The effect of different container types on synthesizing monoliths was also studied. The synthesized crack-free monoliths were characterized using X-ray diffraction (XRD), nitrogen adsorption/desorption isotherm (BET), pore size distribution curve, transmission electron microscopy (TEM), and scanning electron microscopy (SEM). Finally, using the synthesized monoliths, the phase behavior change in a confined system was studied. For single component phase behavior experiments, a differential scanning calorimetry (DSC) and thermogravimetric analysis (TGA) were used. The

synthesized monoliths saturated with decane were used to obtain DSC and TGA profiles.

From these results, the temperature of the phase change in a confined system was shown.

Also, the experimentally measured saturation pressure of the hydrocarbon mixture

(decane-methane) in the nano-sized porous media was obtained from a pressure-volume

graph. To be a standard for the saturation pressure of a bulk system, the phase diagram of

the binary mixture of decane and methane (90:10 mole ratio) was modelled using a

commercial reservoir simulator, CMG (Computer Modelling Group). By comparing the

saturation pressure results with the monoliths to the bulk, the phase behavior change was

shown when they are confined.

3.2 Materials and Methods

3.2.1 Synthesis of the silica-based monoliths

A procedure to synthesize SBA-15 was altered to create the silica-based

monoliths.[46] The chemicals required to synthesize these monoliths are 2 M hydrochloric

acid (HCl), deionized water (DI water), poly(ethylene glycol)-block-poly(propylene

glycol)-block-poly(ethylene glycol) (Pluronic P123), and tetraethyl orthosilicate (TEOS).

The first step in this process is to create a mixture of 120 mL of 2 M HCl and 30 mL of

deionized water (DI water). Then, approximately 4 g of Pluronic P123 were dissolved in

the HCl water solution. When the solution was fully dissolved, 9.1 mL of TEOS were

added and allowed to mix for about 15 minutes. This solution was then poured into a

container or mold. Paraffin film was placed on top of the containers and some holes were

poked in the paraffin film using a needle. Then, the solution was placed into an oven at

50 °C. The monolith solution was left in the oven for varying times depending on the size

of the containers. The smaller the container, the less time the monolith required to form perfectly. This is important because the monoliths will shrink after the optimum synthesis time; determining the optimum synthesis time was a key finding in this work. Various containers and molds were tested to see which was best to synthesize the monoliths. The containers that were tested were made from glass, polyethylene, polycarbonate, and silicone. The dimensions of the various containers and their optimum synthesis times are as follows: 4 days of optimum synthesis time for 100 mL of glass beaker, the polypropylene square food container (62 mm on the top, 51 mm of the bottom, 64 mm of height); 2 days of optimum synthesis time for the glass vial (25 mm diameter and 64 mm of height); and lastly, 1 day of optimum synthesis time for the polyethylene vial (13 mm of diameter and 51 mm of height), the silicone ice cube molds, and the polycarbonate tubing (10 mm of diameter and 160 mm of height).

3.2.2 Characterization

XRD patterns were recorded using X-ray powder diffraction (Bruker D2 Phaser XRD). N_2 adsorption/desorption isotherms were obtained using a sorptometer (Gemini 5, Micromeritics) at 77 K. The synthesized monoliths were calcined at 500 $^\circ$C for 3 hours and degassed at 250 $^\circ$C for 6 hours (3 x 10^{-3} torr), prior to adsorption. The specific surface areas of the samples were calculated by using the BET method and pore size distribution were calculated by the Barrett-Joyner-Halenda (BJH) method. Pore images of monoliths were examined by transmission electron microscopy (FEI Tecnai 12 Transmission Electron Microscope). Morphological features were examined by scanning electron microscopy (FEI Nova Nano FEG-SEM 630).

3.2.3 Simulation

The phase diagram of the binary mixture of decane and methane with 90:10 mole ratio was modeled with the Winprop module of a commercial reservoir simulator, CMG. The Peng-Robinson (1976) equation of state was applied. It is generally superior in predicting liquid densities, especially nonpolar ones. The simulated results were used as a standard of the saturation pressure of the bulk (no nano-sized pores) fluid. From the phase diagram of the mixture of decane and methane with 90:10 mole ratio, the expected saturation pressures at 38 $^{\circ}$C and 52 $^{\circ}$C were shown to be 2620 kPa and 2896 kPa, respectively.

3.2.4 Differential Scanning Calorimetry (DSC) and Thermogravimetric

Analysis (TGA)

The Netzch DSC analyzer, DSC3500, was used for the single component phase behavior experiments. Analyses were performed with the synthesized monoliths saturated with a single hydrocarbon component, decane. BET analysis provided the pore volume of the synthesized monoliths. Based on this pore volume, synthesized monoliths saturated with excess decane (ca. 200%) were prepared. The decane (anhydrous, $\geq$ 99%) from Sigma-Aldrich was used. To prepare the DSC sample, the synthesized monoliths were calcined at 500 $^{\circ}$C for 3 hours. Then, the calculated amount of decane was put in a container where the prepared monoliths were. The sample was kept undisturbed for 48 hours so that the pores were filled with decane by capillary wetting.

The TA Instrument, Q600, was used for another single component phase behavior experiment. TGA analyses were also performed using excess solvents (decane). DSC

and TGA profiles for these materials were measured at atmospheric pressure (86.87 kPa

in Salt Lake City, Utah) in the direction of increasing temperature at a heating rate of 10

^{o}C per minute. Nitrogen atmosphere was employed in the TGA experiments.

3.2.5 Saturation pressure measurement

An apparatus customized for this research was used to measure saturation

pressures (see the Figure 3.1). A 160 mm long transparent tubing with 10 mm outer

diameter and 1.6 mm wall thickness was connected to two high-pressure syringe pumps

(ISCO pumps)—one for decane and one for water—, two gas cylinders of methane and

nitrogen, and a vacuum pump. This system was positioned in an oven. A data acquisition

system was connected to the system in order to record the pressure and volume of the

system using Labview. After injecting the decane into the system, a calculated amount of

methane with the specific mole ratio (90:10 for decane:methane) was injected into the

system. Volume required was calculated using density of decane at temperature of

interest. The specific moles of methane (0.00142 moles) were then introduced into the

system. The pressure requirement for the remainder of the pore volume in the cell was

determined using an equation of state. To increase the contact area between methane and

decane, the methane was injected from the bottom of the tube having decane on the

bottom. The temperature of the oven was raised to two experimental conditions, 38 ^{o}C

and 52 ^{o}C. After the temperature in the oven was steady and no longer fluctuating, the

pressure of the system was raised by adding water continuously to the system at a rate of

0.1 mL/min. Once the pressure reached 8300 kPa, the pressure of the system was

decreased by withdrawing water at a rate of 0.1 mL/min to make sure they reach

equilibrium at each pressure point. From the extrapolated pressure-volume graph, the saturation pressure can be estimated. The pressure where the slope of PV graph dramatically changes is the saturation pressure. Matlab was used, applying regression techniques keeping the R-squared value higher than 0.98. For the experiment with the monoliths, the same procedures were repeated with the grown monoliths in the tubing with filters and filter papers on both ends of the tube. It should be noted that the monolithic silica cores are somewhat compressible, and that may affect saturation pressure measurement results.

3.3 Results and Discussion

3.3.1 Creation of the crack-free monoliths

In this work, the silica-based mesoporous monoliths were synthesized in various containers by controlling the evaporation rate in a mild way. The paraffin film covered the container and holes were created in the paraffin film using a needle, and it allowed the evaporation rate of solution to be controlled from 1.2 to 0.4 g/cm^2. The mesoporous monoliths were synthesized in glass, polypropylene, polyethylene, polycarbonate, and silicone to find the effective types of containers in which silica-based mesoporous monoliths could be synthesized. The monoliths were synthesized well in all containers used.

Figure 3.2 shows that the synthesized monoliths formed and shrank after the specific synthesis time. This shrinkage occurs in all containers, glass, polypropylene, polyethylene, polycarbonate, and silicone, which synthesized the monoliths well. This specific synthesis time before shrinkage is the optimum synthesis time. The optimum

synthesis time depends on the dimensions of the synthesis container. Since large shrinkage was a problem when these monoliths were synthesized, finding an optimum synthesis time is important. To figure out the shrinking process of the monoliths after their optimum synthesis time and the importance of our new synthesis method controlling evaporation rate, the mesoporous monoliths were synthesized with various synthesis times. As shown in Figure 3.2, the synthesized monoliths, following our new synthesis method, have the optimum synthesis time, 2 days for the glass vial with 25 mm of diameter and 64 mm of height. After its optimum synthesis time, the monoliths started to shrink. The monoliths shrank more as time goes by.

Figure 3.3 shows the synthesized monoliths at their optimum synthesis time. Their shapes are the exact same as the container that was used to synthesize them. According to the sol-gel process theory, the stress that causes cracking is mainly attributed to the internal pressure gradient.[60–63] During the evaporation process, the vapor phase and the liquid phase exist simultaneously in the pores of the silica gel. If the evaporation rate is relatively high and the gel loses its permeability, an internal pressure gradient will form inside the silica gel and cracking will start from the flaws at the gel surface to reduce this pressure gradient.[60] Also, during the evaporation process, fluid from pores of different diameters evaporates at different rates. The larger pores empty first, and then they will be shrunk under the capillary pressures of nearby pores that are saturated with liquid. Inhomogeneous capillary forces could cause cracks from the flaws at the surface. In this work, the paraffin film helped control the evaporation rate, so that the internal pressure gradient was reduced. At the same time, the capillary pressure imbalance was reduced. As a result, the shrinkage of the monoliths was prevented

following our synthesis approach.

The monoliths were also synthesized well in the polyethylene vials (see Figure 3.4). The time that monoliths can be synthesized well depends on the cross-sectional area of the container. Since the cross-sectional area of the polyethylene vial was 1.3 cm^2, which was smaller than the glass vials (4.9 cm^2), it took a day to be optimized rather than 2 days. Also, the evaporation rate following our synthesis approach in polyethylene vial was the same with the glass vials.

Figure 3.5 shows the importance of controlling the evaporation rate for synthesizing monoliths. The monoliths shrank dramatically when synthesized without the paraffin film. The monoliths synthesized without controlling evaporation rate do not have an optimum synthesis time.

As shown in Figure 3.6, the monoliths were synthesized well in silicone ice cube molds. This shows that the monoliths can be synthesized without cracks using the paraffin film in various shapes that are dictated by the molds. Based on these synthesis results, the synthesized monoliths were prepared in polycarbonate tubing, with filters and filter paper on both ends of the tube for saturation pressure measurement. As shown in Figure 3.7, there is no gap between the monolith and the polycarbonate tubing and it has no crack. The optimum synthesis time of this monolith, synthesized in the polycarbonate tubing, is a day.

3.3.2 Characterization

The synthesized monoliths were characterized thoroughly using XRD, N_2 adsorption/desorption isotherms, pore size distribution, TEM, and SEM. As shown in

Figure 3.8, X-ray patterns of the synthesized monoliths show four peaks that can be indexed as (100), (110), (200), and (210) diffraction peaks associated with *p6mm* hexagonal symmetry.[46,64] This X-ray pattern matches well with the one of SBA-15, which is one of the mesoporous materials that can be synthesized using the same reactants as the silica-based monoliths. The monoliths were synthesized with the exact size of the desired container, but SBA-15 has particle sizes of 1-10 μm. The d spacing of the synthesized monoliths can be calculated by Bragg's law. The intense (100) peak reflects a d spacing of 104 Å, and three other peaks (110), (200), (210) reflect 54 Å, 49 Å, and 34 Å, respectively. This information also matches well with that of SBA-15.[46]

As shown in Figure 3.9, the nitrogen adsorption/desorption isotherms of the synthesized monoliths match well with type IV isotherms. A pure mesoporous material generally has a hysteresis loop in its nitrogen adsorption/desorption isotherms, and it is associated with capillary condensation and evaporation taking place in its inner pores. The gas condenses in the pores to a bulk liquid phase by capillary condensation. The gas in pores with different diameters will condense at different pressures, and this can give us information about the distribution of pore sizes present in the samples.[52] The nitrogen adsorption/desorption isotherms of the synthesized monoliths have a hysteresis at the relative pressure in the range of 0.6-0.8. The synthesized monoliths have a 621 m^2/g of BET specific surface area and a 0.71 cm^3/g of pore volume. This BET specific surface area is high enough when compared to that of SBA-15. The pore size distribution of the synthesized monoliths is shown in Figure 3.10. The pore size distribution curve was obtained from the nitrogen adsorption/desorption isotherms. The pore size distribution curve has one sharp peak around 6 nm, which is similar to the one of SBA-15. The

average pore size of the synthesized monoliths calculated by BJH method was 5.8 nm.

The TEM images of the synthesized monoliths show highly ordered, aligned, one-dimensional channel structures (see the Figure 3.11). Also, from the TEM images, the distance between the mesopores was shown, and it is estimated to be about 10 nm, which is similar to the shale reservoirs and in agreement with that determined from the XRD data. To prepare the monoliths for TEM imaging, the synthesized monoliths were ground with methanol using an agate mortar and pestle. Once they were dispersed in the methanol as small particles, they were transferred with a graduated transfer pipet and dropped on the TEM grid. Once they were dried, they were ready for TEM imaging. SEM image shows us the mesopores on a coarser resolution (see the Figure 3.12). For the SEM sampling, the synthesized monoliths were fully dried. A small amount of the sample was placed on the SEM specimen holder, held by a small piece of adhesive carbon tape. The SEM image of the monoliths shows that the monoliths are comprised of nano-sized pores. All characterization results of the synthesized monoliths matched well with the references of SBA-15.[40,64]

3.3.3 Phase behavior change measurements

3.3.3.1 Differential scanning calorimetry (DSC)

Isobaric (atmospheric pressure) DSC thermograms of decane in the synthesized monoliths were performed for a single component phase behavior experiment in a nano-sized porous media. To see the effect of nano-sized pores on phase transition temperature, the DSC profile of decane in silicon dioxide (SiO_2) powders was determined, as well. SiO_2 (Sigma-Aldrich) has pores with larger than micron size. The

DSC profile of bulk decane (without porous media) is presented as the bottom trace, the DSC profile of decane in SiO_2 is shown in the middle, and the one of decane in the synthesized monoliths is shown as the top trace in Figure 3.13. For pure decane, the bulk-vaporization peak is observed at the boiling point of decane.[65] The DSC profile of decane in SiO_2 has one peak at the same temperature, which is the boiling point of decane. However, the confined decane in the monoliths with nano-sized pores exhibited two endothermic peaks. This result matches with the previous literature of Luo et al.[9,29,30] The first peak appeared at a temperature slightly below the bulk vaporization temperature and the second peak was observed at a temperature higher compared to the bulk vaporization peak. It is difficult to establish association of peaks with bulk or confined fluid without additional information. The first peak may be associated with bulk vaporization and the second with fluid in the confined pores, if the sample was hydrophobic. Wettabilities of the monoliths were not measured. However, SBA-15 powders were synthesized using the same reactants as the monoliths. SBA-15 was shown to have a high strength of adsorption with toluene and isopentane, according to Serrano et al.[44] This shows that SBA-15 is primarily hydrophobic. From comparison of three DSC profiles, phase behavior change of the confined fluid in nano-sized pores was shown.

3.3.3.2 Thermogravimetric analysis (TGA)

TGA profiles of pure decane and the decane in monoliths were shown in Figure 3.14. For the TGA experiments, a crucible open to the atmosphere was used. Liquids evaporate in open crucibles over a wide temperature range below their boiling point. This may be one reason why the weight loss begins at temperatures below the boiling point of

decane. The temperature of weight loss of decane in monoliths started at lower

temperature than bulk decane. The derivative graph of two TGA profiles is also shown in

Figure 3.14 which shows the temperature range of the weight loss of decane in monoliths

was lower than the one of pure decane. These results match well with the DSC results in

Figure 3.13.

3.3.3.3 Simulated phase diagram of two components

The phase diagram of the binary mixture of decane and methane with a 90:10

mole ratio was modeled with the Winprop module of the CMG reservoir simulator (see

Figure 3.15). Real reservoir fluids contain many more than one. That is the reason why

the mixture of decane and methane was chosen for the experimental reservoir fluids.

Figure 3.15 shows the pressure-temperature phase diagram for a mixture of decane and

methane with 90:10 mole ratio. This pressure-temperature phase diagram gives the region

of temperatures and pressures at which the mixtures form two phases. Up to the

cricondentherm, two phases are formed. At temperatures greater than the cricondentherm,

only one phase occurs, regardless of pressure. In other words, if the hydrocarbon mixture

is in a reservoir at a temperature and pressure on the right side of the envelope, a decline

in pressure at approximately a constant temperature caused by the removal of fluid from

the reservoir would not cause the formation of a second phase. However, if the

hydrocarbon mixture is in a reservoir at a temperature between the critical temperature

and the cricondentherm, the production of fluid from a reservoir starting at the point

above the envelope causes liquid to appear in the reservoir when the dew-point pressure

is reached. With a reservoir in which the temperature is less than the critical temperature,

isothermal pressure reduction from the point above the envelope causes the appearance of vapor phase at the bubble point pressure.[66] Thus, the bubble points of the reservoir fluids are important properties that determine the relative amounts of fluids produced. Determining the dew point and bubble point depends on where the critical points are on the envelope. As shown in Figure 3.15, the critical point for the mixture of decane and methane with 90:10 mole ratio is at 344 ^{o}C and 3447 kPa. The experimental temperatures used in this research were 38 ^{o}C and 52 ^{o}C, which are well below the critical temperature. Therefore, the gas phase will appear once the pressure reduction reaches the bubble point, and that is how a bubble point is going to be determined from the experiments. The simulated saturation pressure of the methane and decane mixture with 90:10 ratio is 2620 kPa at 38 ^{o}C and 2896 kPa at 52 ^{o}C. The saturation pressure increases when temperature increases.

3.3.3.4 Saturation pressure measurement

The experimental saturation pressures were estimated from a PV graph from the saturation pressure measurement experiment. The saturation pressure is the pressure where the slope of the PV graph changes dramatically.[51] As shown in Figure 3.16, the pressure at which there was significant slope change was found from the experimental PV graph of the bulk sample at two different temperatures. Matlab was used to get the exact saturation pressure from the PV graph, and the results match well while having an R-squared value higher than 0.98.

As shown in Table 3.1, the saturation pressures, where the slope of PV graph changes dramatically, of the methane and decane mixture with 90:10 mole ratio are 2547

kPa at 38 ^{o}C and 2751 kPa at 52 ^{o}C (average values). Bulk experiments were repeated. Standard deviations are shown in Table 3.1. The experimentally measured saturation pressure increases when temperature increases from 38 ^{o}C to 52 ^{o}C. The experimental results have a good agreement with the simulated results at different temperatures. The experimental bulk results are the standard because they are close enough to the simulated results. Therefore, the experimental saturation pressure with monoliths can be compared to the experimental standard bulk results.

All experimentally measured PV graphs with the synthesized monoliths have the same shape as the PV graph with the bulk results (see Figure 3.17). The saturation pressures measured with the monoliths at two different temperatures are shown in Table 3.1. The experimental saturation pressure results with the monoliths are 2037 kPa at 38 ^{o}C (average value) and 2296 kPa at 52 ^{o}C. Experiments at 38 ^{o}C were repeated by synthesizing new monoliths. The measured saturation pressures with the monoliths at the different temperatures were lower than the bulk results about 21%. From these results, the effect of nano-sized pores on the saturation pressure was confirmed.

3.4 Conclusions

Bubble points of hydrocarbon in low-permeability formations are important in understanding the relative amounts of gas and liquid flows and thus are an important component in establishing the economics of production. Bubble point measurements in well-calibrated mesoporous media consisting only of nano-sized pores will provide fundamental understanding of how hydrocarbon bubble points are affected by their presence in shale type environments. Mesoporous silica monoliths consisting only of

nano-sized pores are good analogs to study this hydrocarbon behavior. It is difficult to synthesize crack-free monoliths which can be used for these studies. Crack-free monoliths were synthesized in desired enclosures by using a controlled evaporation process. In the polycarbonate pressure tube, where saturation pressure measurements were conducted, the evaporation rate of mixtures used in the synthesis was 0.4 g/cm^2

The BET-specific surface area of the synthesized monoliths was 621 m^2/g, the pore volume was 0.71 cm^3/g, and the average pore size calculated by the BJH method was 5.8 nm. This pore size matched well with the pore size distribution curve displaying one peak around 6 nm. The porous structure of the synthesized monoliths was shown in the TEM images as well. DSC thermograms of the synthesized monoliths with saturated decane showed two peaks because of the confinement effect. One was at a temperature lower than the boiling point of bulk decane and the second one was at a higher temperature than the bulk decane. TGA profiles showed that evaporation of decane in the monoliths occurred at the lower temperature than the one with decane. The experimentally measured saturation pressures of bulk decane-methane mixtures at two different temperatures matched well with the simulated results. The experimentally measured bubble point pressures of decane-methane mixtures in the monoliths were lower than the bulk results. The results in this chapter show that the presence of hydrocarbon mixtures in mesoporous media characterized only by the presence of nano-sized pores may lead to bubble point suppression.

Table 3.1 Experimental saturation pressure results for 90% decane and 10% methane with the synthesized monoliths and without (bulk). Bulk measurements are provided for comparison.

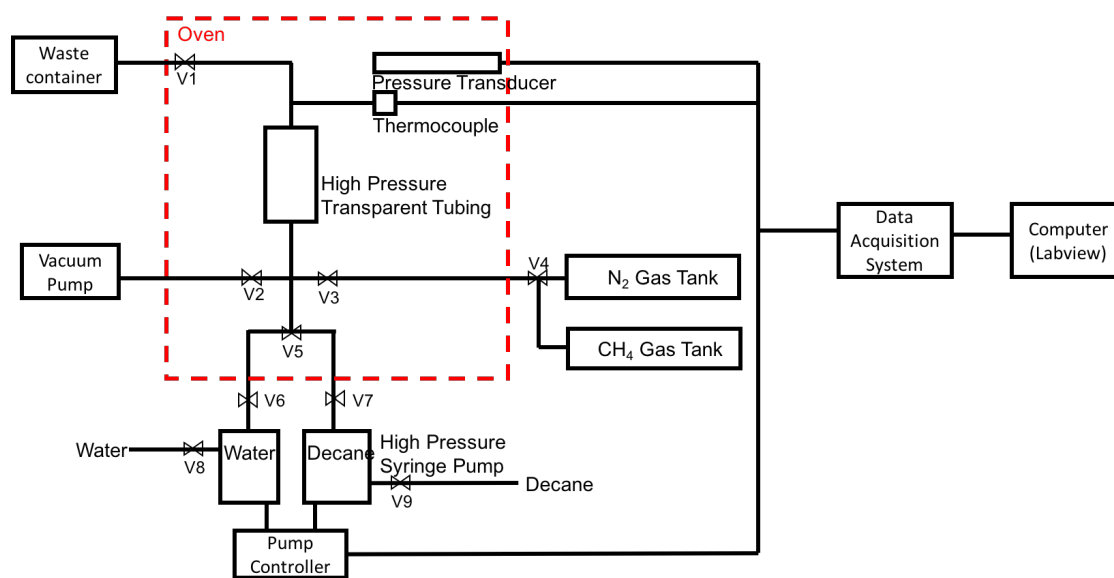| Temp. (°C)	Saturation pressure (kPa)					
	Simulated	Bulk			Monoliths	
		Experiments		SD[1]	Experiments	SD[1]
38	2620	1st	2579	46	1st	2144	69
		2nd	2481		2nd	1979	
		3rd	2579		3rd	2096	
52	2896	1st	2717	44	2296	
		2nd	2723			
		3rd	2813			

[1]Standard Deviation

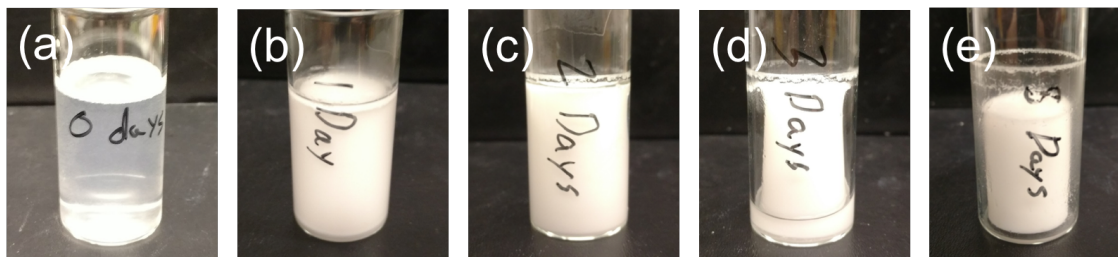Figure 3.1 Saturation pressure measurement system overview.

Figure 3.2 Photos of the monoliths synthesized in a glass vial from the beginning to 8
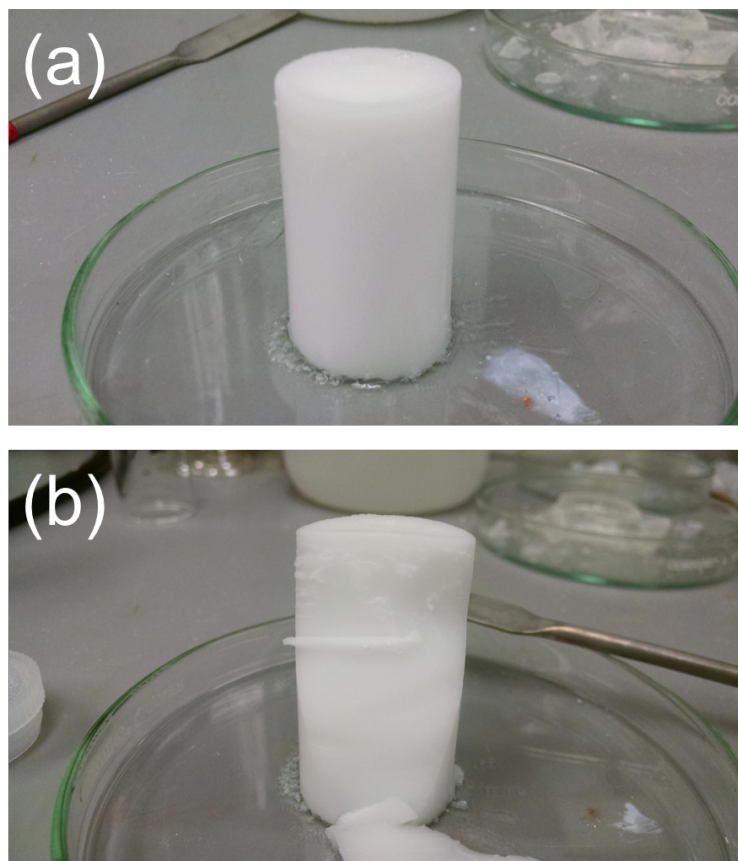
days.

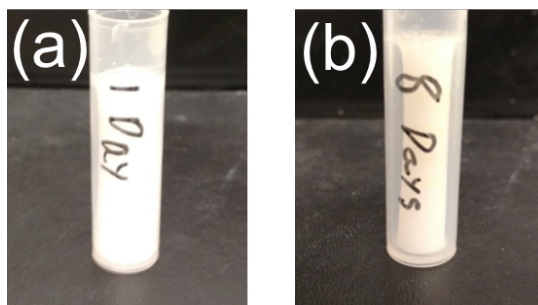Figure 3.3 Photos of the synthesized monoliths at 2 days.

Figure 3.4 Photos of the monoliths synthesized in polyethylene vial at 1 day and 8 days.
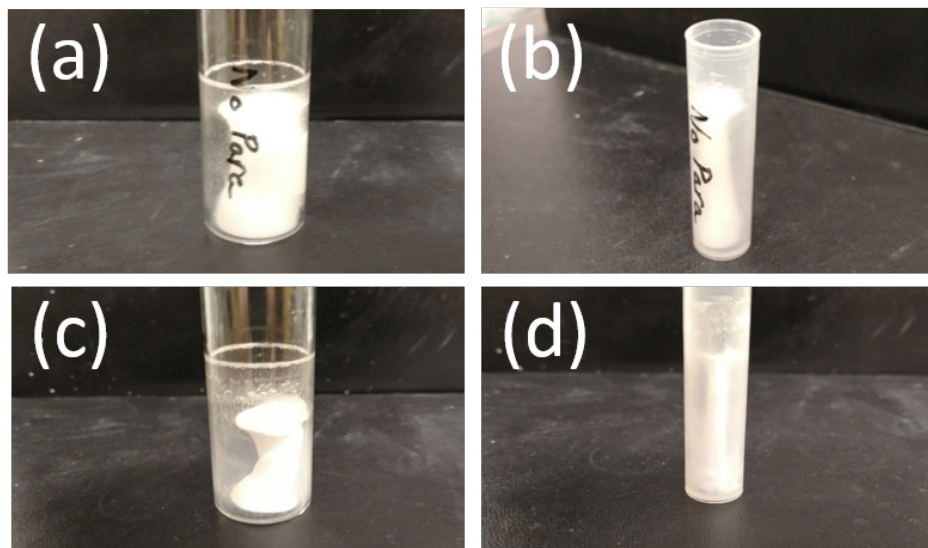
Figure 3.5 Photos of the monoliths synthesized without controlling the evaporation rate in

a glass vial and polyethylene vial: (a) and (b) at 2 days, and (c) and (d) at 8 days.

Figure 3.6 Photos of the monoliths synthesized in a silicone ice cube.

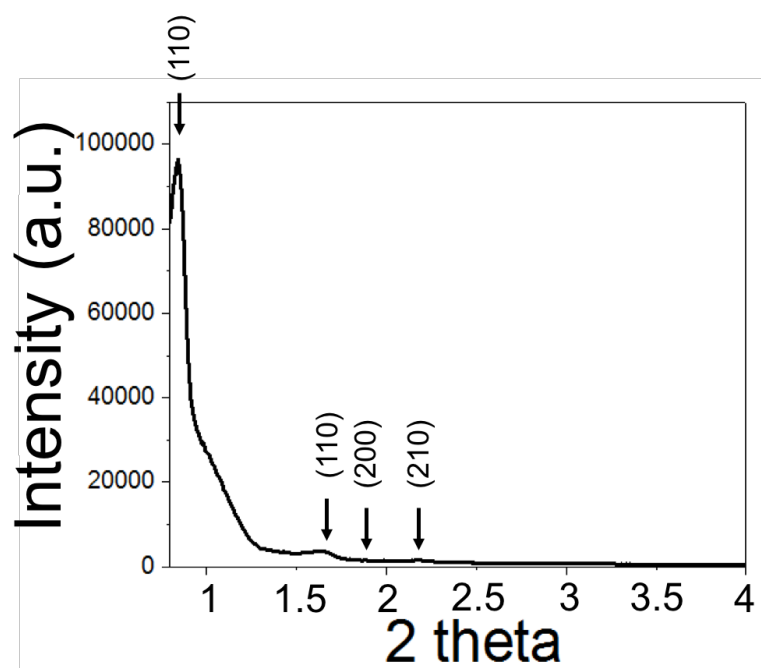Figure 3.7 Photo of the grown monoliths synthesized in a polycarbonate tube.

Figure 3.8 X-ray diffraction of the synthesized monoliths.
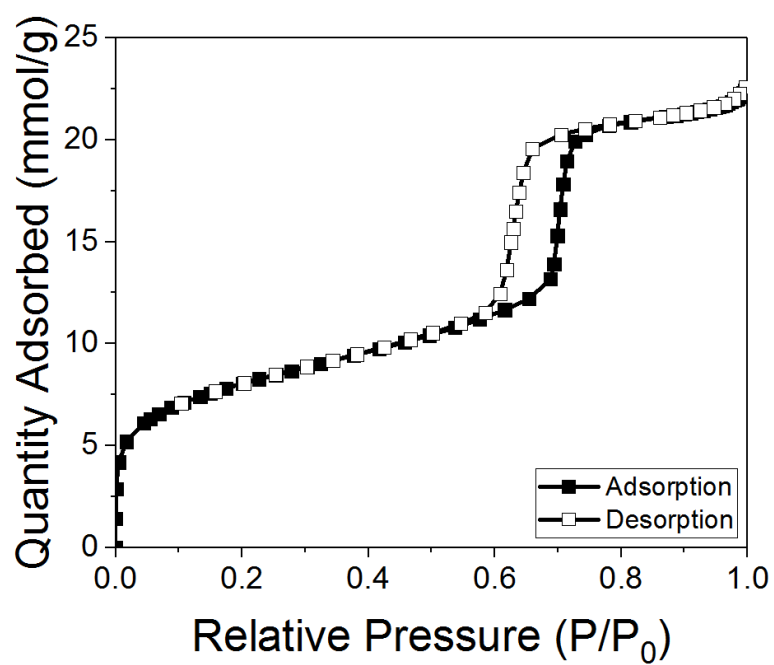
Figure 3.9 N_2 adsorption/desorption isotherms of the synthesized monoliths.
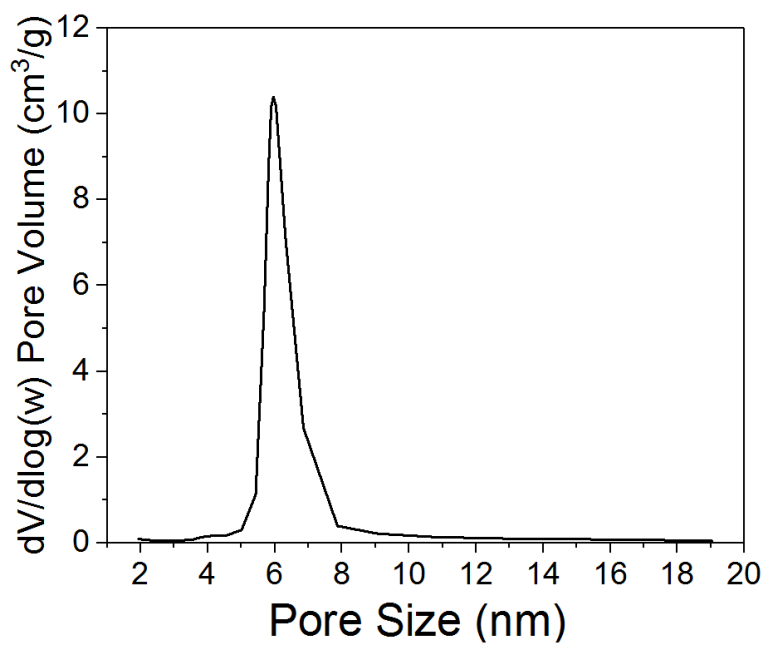
Figure 3.10 Pore size distribution curve of the synthesized monoliths.
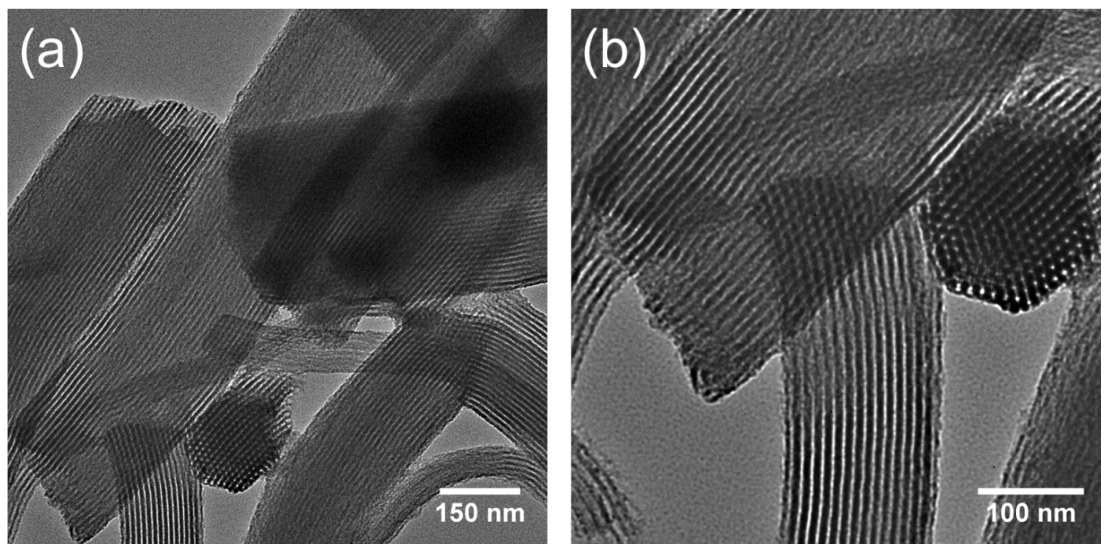
Figure 3.11 TEM images of the synthesized monoliths.

| det | mode | HV | curr | mag □ | HFW | ⊢————— 20 μm ————⊣ |
| ETD | SE | 1.00 kV | 25 pA | 8 000 x | 51.8 μm | Monoliths |
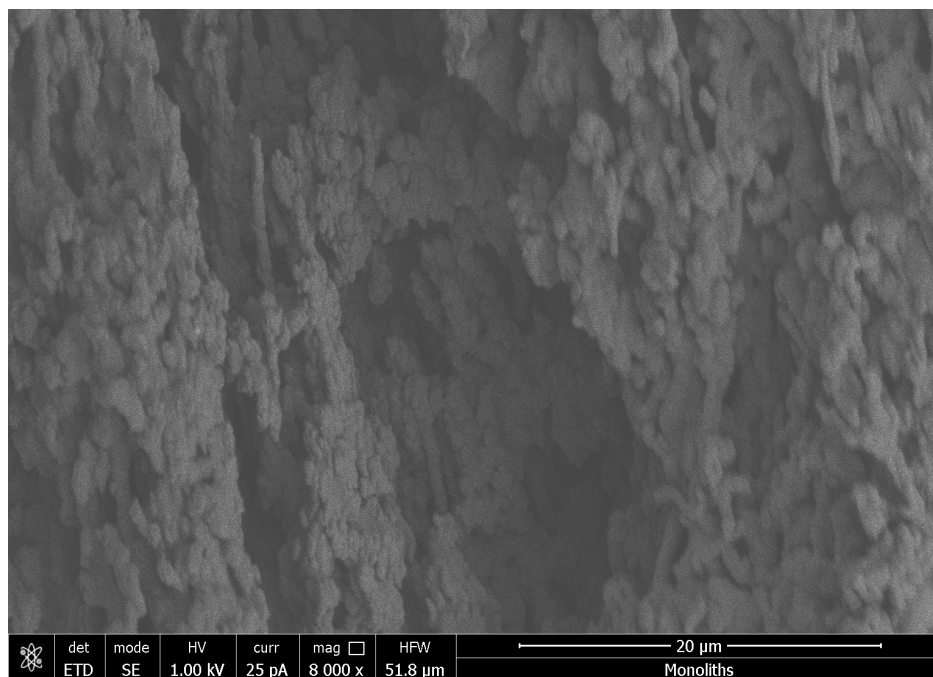
Figure 3.12 SEM image of the synthesized monoliths.
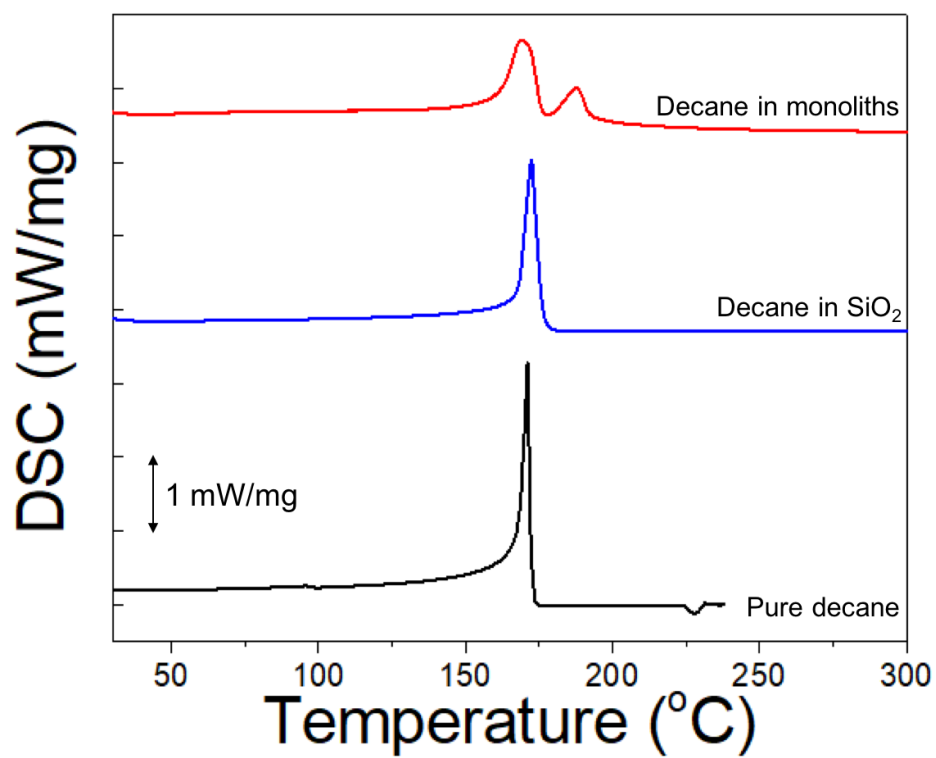
Figure 3.13 DSC profiles of pure decane and decane in the monoliths.
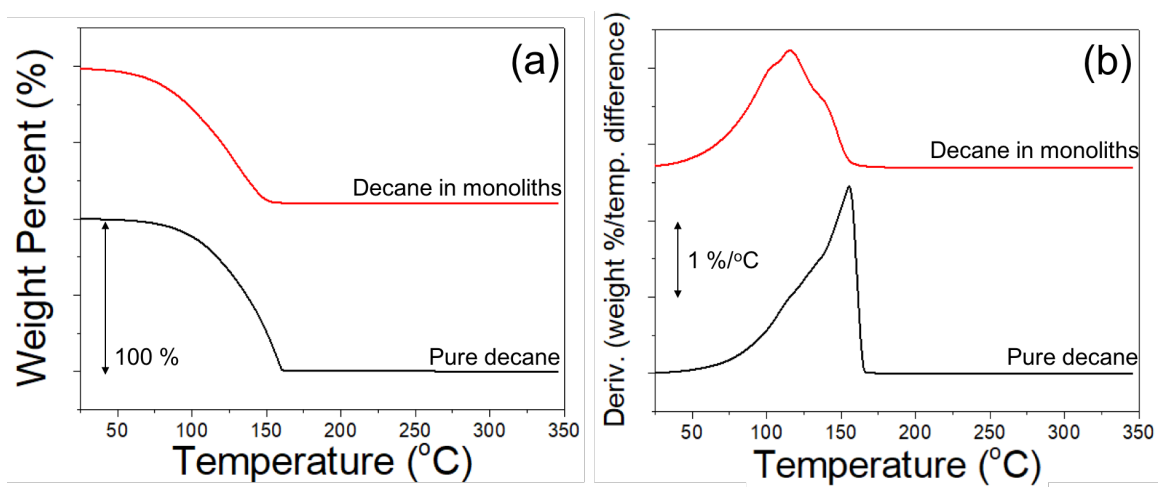
Figure 3.14 TGA profiles (a) and their derivative graphs (b) of pure decane and decane in

monoliths.
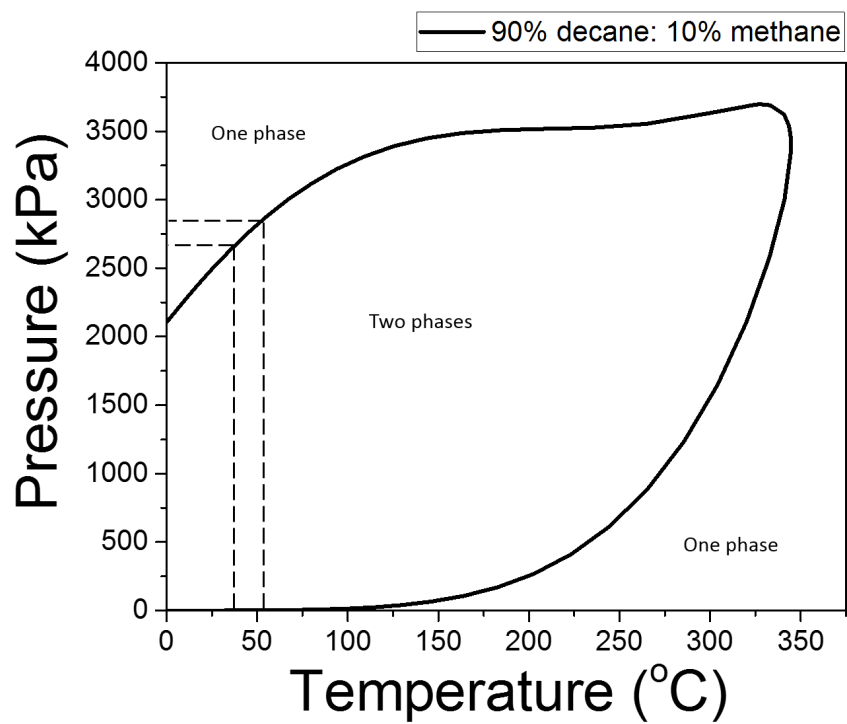
Figure 3.15 Pressure-temperature (P-T) plot of the 90% decane and 10% methane molar

mixture obtained using a thermodynamic program employing the Peng-Robinson

equation of state.
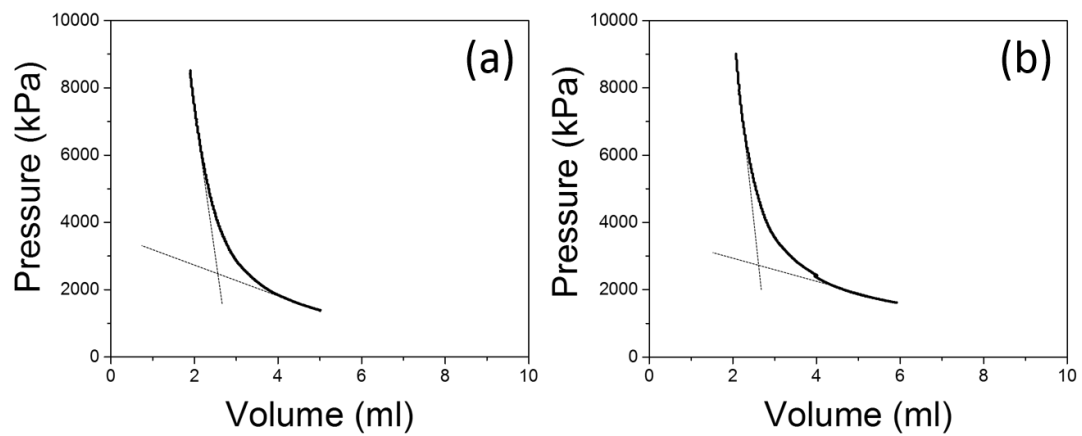
Figure 3.16 Experimentally measured pressure-volume plots for the 90% decane and 10% methane molar mixture at 38 ^{o}C (a) and 52 ^{o}C (b).
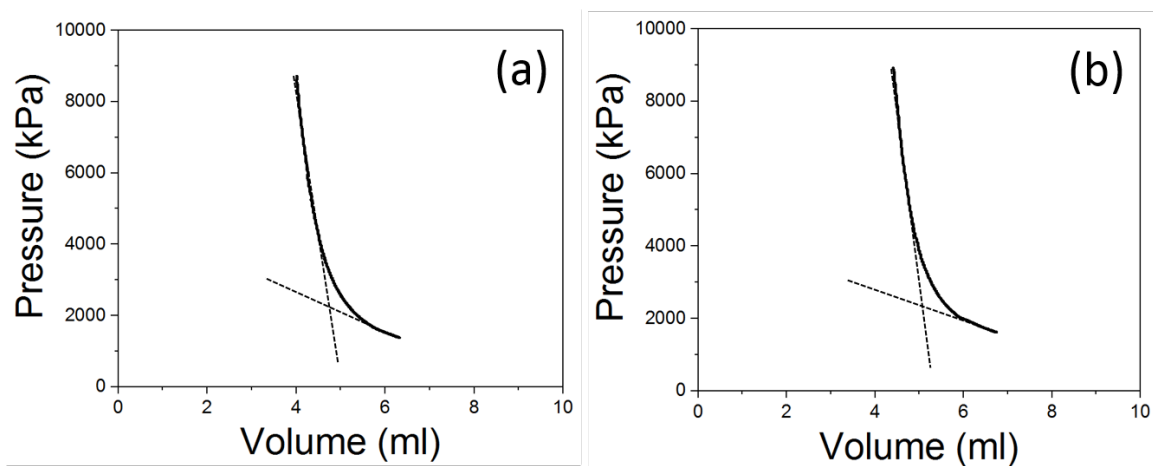
Figure 3.17 Experimentally measured pressure-volume plots for the 90% decane and 10% methane molar mixture in the synthesized monoliths at 38 °C (a) and 52 °C (b). The change in slope with an increase or a decrease in the volume indicates a phase transition.

CHAPTER 4

BUBBLE POINT MEASUREMENTS OF A HYDROCARBON MIXTURE

IN A NIOBRARA SAMPLE FORMATION

4.1 Introduction

As oil and gas production from conventional reservoirs has declined, shale

reservoir development has become a hot topic worldwide. However, reservoir fluid phase

behavior is still poorly understood due to the complexity of the porous system comprising

these shale reservoirs. Common features of the shale reservoirs include their extremely

small pore size, nanometer in scale, and, hence, low permeability (at the nanodarcy

level). In low-permeability formations, interfacial phenomena are prominent because of

the fine grains and small pores. In Chapters 2 and 3, the effect of nano-sized confinement

on bubble point was studied using several synthesized siliceous mesoporous materials.

All of the results and conclusions from the studies were in accordance with theoretical

derivations or hypotheses for a nano-sized confinement. Nevertheless, it is still a

challenge to accurately measure such phase behavior changes in nano-sized porous rock.

A shale reservoir typically consists of mudrock with a very fine-grained rock texture.[14,27]

Mineralogic components are a mixture of silicate minerals, calcite, clays, organic matter,

etc.[67] These rock fragments have a wide range of pore sizes, from nanometer pores to

macrometer pores. Understanding the phase behavior of hydrocarbons in this complex

system is needed. Once this is studied, then it will be possible to confirm the effect of nano-sized pores on a phase behavior (bubble point) in Chapters 2 and 3.

In this work, the porous characteristics of a Niobrara, outcrop sample were studied using nitrogen adsorption/desorption isotherms and the pore size distribution curve. Niobrara rock is from one of the most productive shale reservoirs in the U.S (see Figure 1.1). Also, the bubble point of a hydrocarbon mixture (decane-methane with 90:10 mole ratio) was measured in the Niobrara rock. This will complete the study about the phase behavior of hydrocarbons in shale reservoirs.

4.2 Methods

4.2.1 Characterization

A N_2 adsorption/desorption isotherm was obtained using a sorptometer (Gemini 5, Micromeritics) at 77 K. The sample was degassed at 523 K for 6 hours (3 x 10^{-3} torr) prior to adsorption. The specific surface areas of the samples were calculated by the Brunauer-Emmett-Teller (BET) equation, and pore size distribution curves were obtained by the Barrett-Joyner-Halenda (BJH) method.

4.2.2 Thermodynamic calculation

The phase diagram of the binary mixture of decane and methane with a 90:10 mole ratio was modeled with the commercial thermodynamic simulator, Winprop of the Computer Modeling Group (CMG). The simulator used the Peng-Robinson equation of state, the accepted method for predicting phase compositions of hydrocarbon mixtures. The bubble point of the decane and methane mixture with a 90:10 mole ratio was

measured at 21 ^{o}C. The thermodynamic calculation using the Peng-Robinson equation of state predicted the bubble point to be 2413 kPa.

4.2.3 Sample preparation

The Niobrara sample was plugged with a core bit (Terra Diamond Industrial) having an inner diameter of 19 mm and a length of 51 mm. This extracted core was placed in a stainless steel tube with an inner diameter of 21 mm. The gap between the core and the tube was filled with epoxy (DP105, 3M Adhesives) using a dispensing gun and a mixer nozzle to simultaneously mix and dispense the epoxy. After 48 undisturbed hours, the epoxy became hard, and the sample was ready to be used for measuring the bubble point.

4.2.4 Bubble point measurement

Bubble point measurements were performed using a specially designed apparatus (see the Figure 4.1). The prepared tube with the rock sample was connected to two high-pressure syringe pumps (ISCO pumps) for decane and water, two gas cylinders of methane and nitrogen, and a vacuum pump. The prepared tubing was placed in an oven. The experimental procedure from Chapters 2 and 3 was repeated using the prepared tube with the rock sample at the temperature of 21 ^{o}C. To compare the results of the mixture in shale with those of bulk mixture, the same procedure was repeated without porous media. From the extrapolated PV graph, the bubble point could be estimated. The pressure where the slope of PV graph dramatically changes is the bubble point. Matlab was used to estimate the bubble point by analyzing data from Labview. The bubble point was

achieved from the regression techniques having R-squared values higher than 0.98.

4.3 Results and Discussion

The nitrogen adsorption/desorption isotherms of the Niobrara sample are shown in Figure 4.2. The shape of the isotherms and their hysteresis pattern provide useful information about the physisorption mechanism. The International Union of Pure and Applied Chemistry (IUPAC) classified the adsorption isotherms into six types, Type I to Type VI, and the hysteresis patterns into four types, Type H1 to Type H4 (Sing 1985).[68] The different hysteresis patterns indicate a different shape of mesopores (Sing 1985). Figure 4.2 shows typical isotherm profiles and characteristics of the Niobrara sample.[67] The N_2 adsorption/desorption isotherms of the Niobrara rock have the shape of Type II isotherms, which are characteristic of nonporous or dominantly macroporous materials. However, the Niobrara isotherms are not purely Type II because they have an H3 type hysteresis loop on the isotherms. This pronounced hysteresis loop indicates there is a significant volume of mesopores. The samples are also not exclusively mesopores as there is no indication of complete mesopore filling because the isotherms lack a plateau at higher relative pressures, such as is typical for the Type IV isotherm. Rouquerol et al. (1999) suggested that these types of isotherms, which are observed in the Niobrara samples, should be designated as new Type IIB isotherms.[69] These Type IIB isotherms are shown from materials having mesopores and macropores.

The Niobrara sample has a BET surface area of 4 m^2/g with 0.006 cm^3/g of pore volume. The average pore size of the Niobrara rock calculated by the BJH method was 6.3 nm. The pore size distribution of the Niobrara rock is shown in Figure 4.3. This pore

size distribution curve was calculated from its N_2 adsorption/desorption isotherms using the BJH method. The pore size distribution of the Niobrara rock has a peak of around 4 nm and keeps increasing. This result describes the character of its N_2 isotherms (Type IIB) and matched well with the calculated average pore size. According to Kuila et al., the Niobrara rock in this study has low clay content (<10 wt.%) in the low organic matter (<3 wt.%) group, based on its N_2 isotherm and specific BET surface area.[67]

The phase diagram of the binary mixture of decane and methane with 90:10 mole ratio modeled with the Winprop of the CMG reservoir simulator is shown in Figure 4.4. The mixture with 90:10 mole ratio has a critical temperature of 344 °C and a critical pressure of 3447 kPa. The upper curve from the critical point is a bubble point curve, and the lower curve from the critical point is a dew point curve. The bubble points were measured at 21 °C, and the phase diagram of the mixture shows the bubble point of the bulk mixture at 21 °C to be 2413 kPa (please see Figure 4.4).

The experimentally measured bubble points were determined from the pressure-volume graph which was obtained from the bubble point measurement experiment. The pressure where the slope of the pressure-volume graph dramatically changes is the bubble point. Figure 4.5 shows the pressure-volume graph of the mixture of decane and methane with 90:10 mole ratio at 21 °C. The bubble point was determined using Matlab, with the regression having R-squared values higher than 0.98. The bubble points obtained using this technique are shown in Table 4.1. Standard deviations are also shown in Table 4.1. The bubble point of the mixture of decane and methane was 2455 kPa at 21 °C in average. This result matches well with the thermodynamic calculation from the CMG reservoir simulator, which was 2413 kPa.

Finally, the experimentally measured bubble point of the mixture in a Niobrara outcrop sample is shown in Figure 4.6. The Niobrara rock is a porous media, with a pore size of 6.3 nm. This porous system was expected to affect the bubble point of hydrocarbon mixture. The shape of the pressure-volume graph from the experiments with the Niobrara rock is similar to that of the bulk graph. As shown in Table 4.1, the average bubble point with the Niobrara outcrop sample is 1979 kPa at 21 $^\circ$C. Comparing the bubble point result of the bulk mixture with the result of the mixture in the Niobrara outcrop sample shows the suppression of the bubble point when hydrocarbon mixtures are in a shale rock.

4.3 Conclusion

The Niobrara outcrop sample was characterized with nitrogen adsorption/desorption isotherms and its pore size distribution curve. The porous system of the Niobrara rock, which is from one of most productive shale reservoirs, was studied. Having mesopores and macropores together, the Niobrara rock's nitrogen isotherms have been shown to be a type. The pore size distribution curve of the Niobrara sample corresponded with its nitrogen isotherms. The bubble point pressures in the bulk were found to be higher than the bubble point pressures of the same fluids confined in the nanometer scale pores. A suppression of 476 kPa in the bubble point of decane-methane (90:10% molar ratio) was observed for the mixture confined in the Niobrara rock. These measurements provided evidence that bubble points of oils are lower in shale reservoirs.

Table 4.1. Bubble points of a mixture of decane-methane with a 90:10 mole ratio with the

Niobrara sample and without (bulk).

Temp. (^{o}C)		Bubble point pressure (kPa)					
	Simulated	Bulk			with Niobrara sample		
		Experiments		SD[1]	Experiments		SD[1]
21	2413	1st	2592	103	1st	2075	83
		2nd	2351		2nd	1986	
		3rd	2413		3rd	1875	

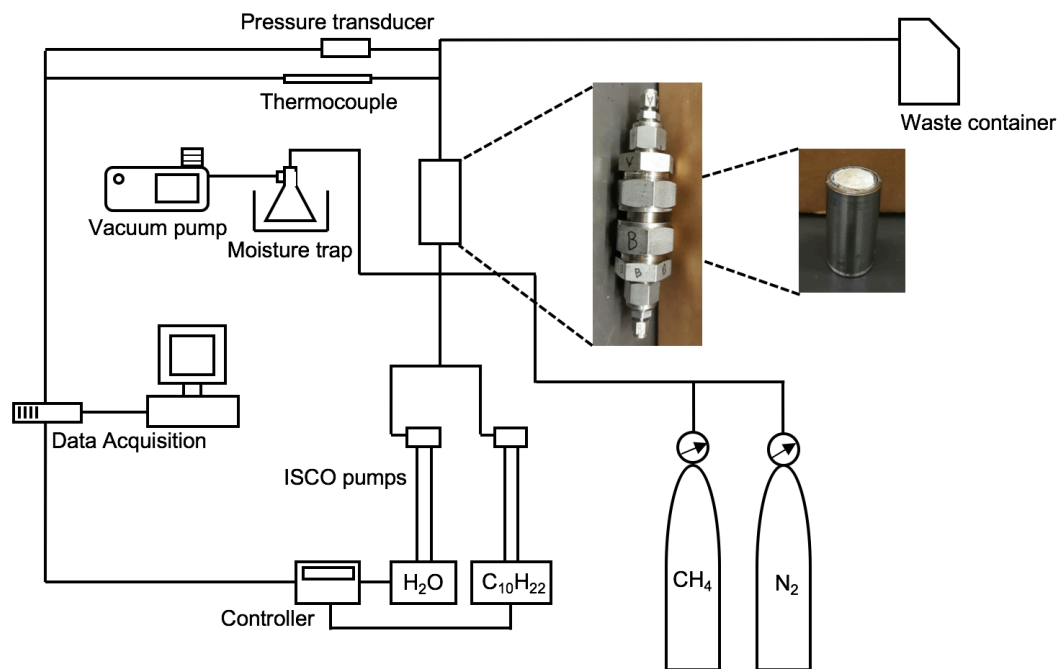[1]Standard Deviation

Figure 4.1 System overview of bubble point measurement for a low permeability rock sample.
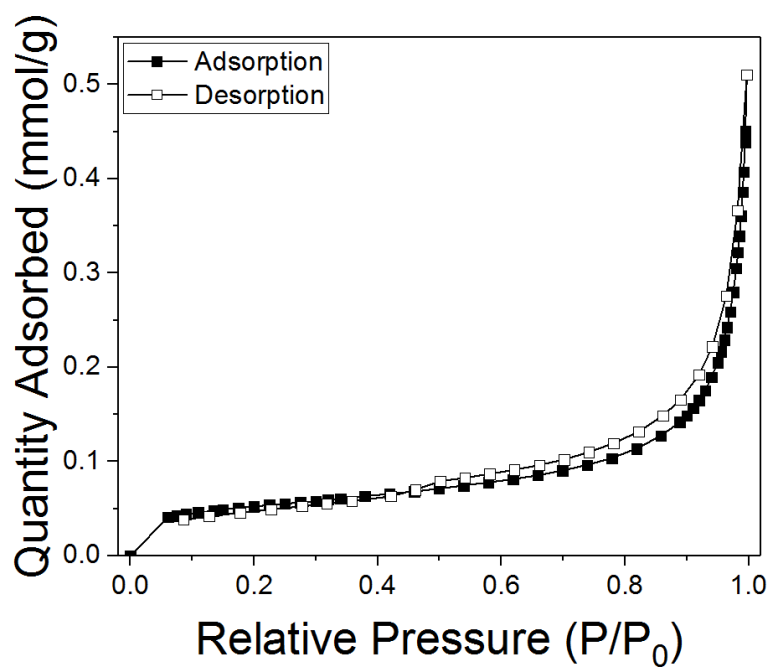
Figure 4.2 Nitrogen adsorption/desorption isotherms of Niobrara sample.
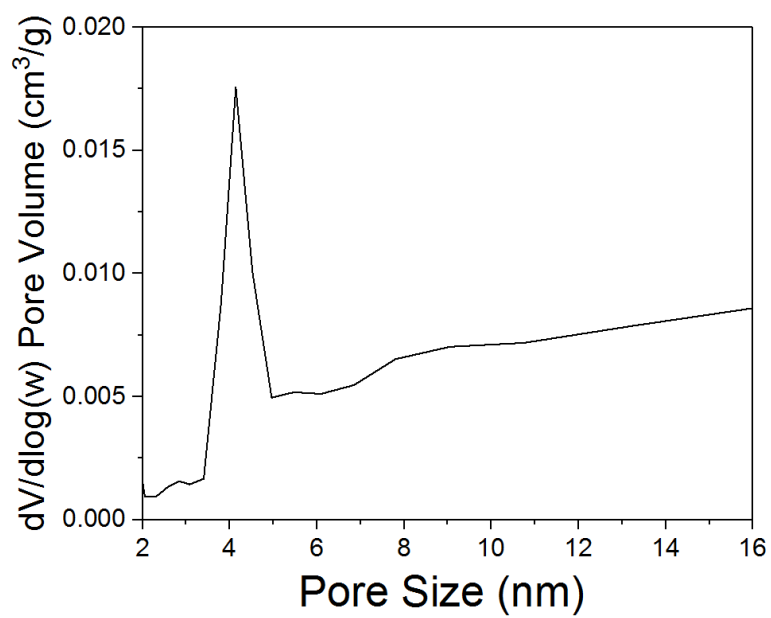
Figure 4.3 Pore size distribution of Niobrara sample.
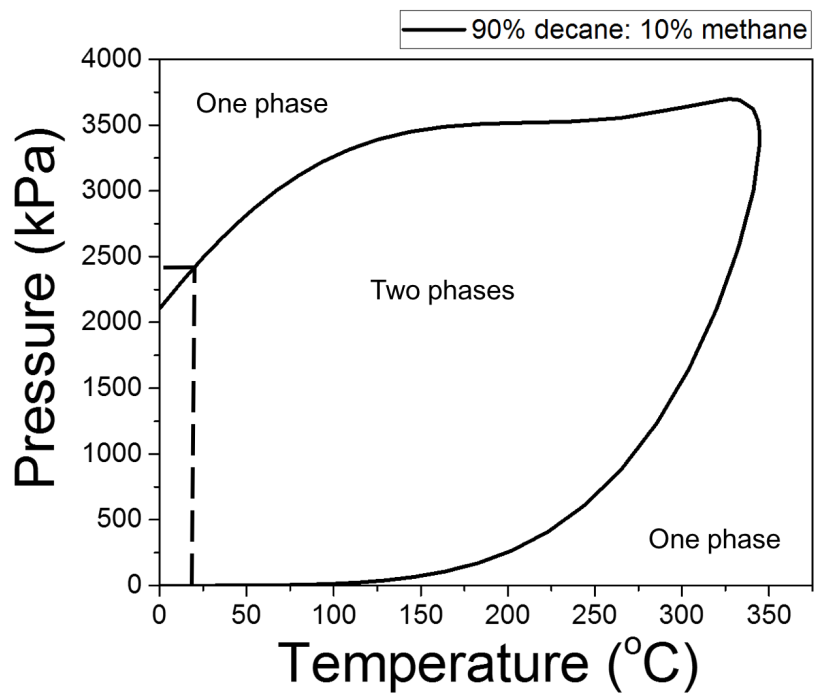
Figure 4.4 Pressure-Temperature graph of the hydrocarbon mixture of decane-methane

with a 90:10 molar ratio calculated by Computer Modeling Group (Winprop module).
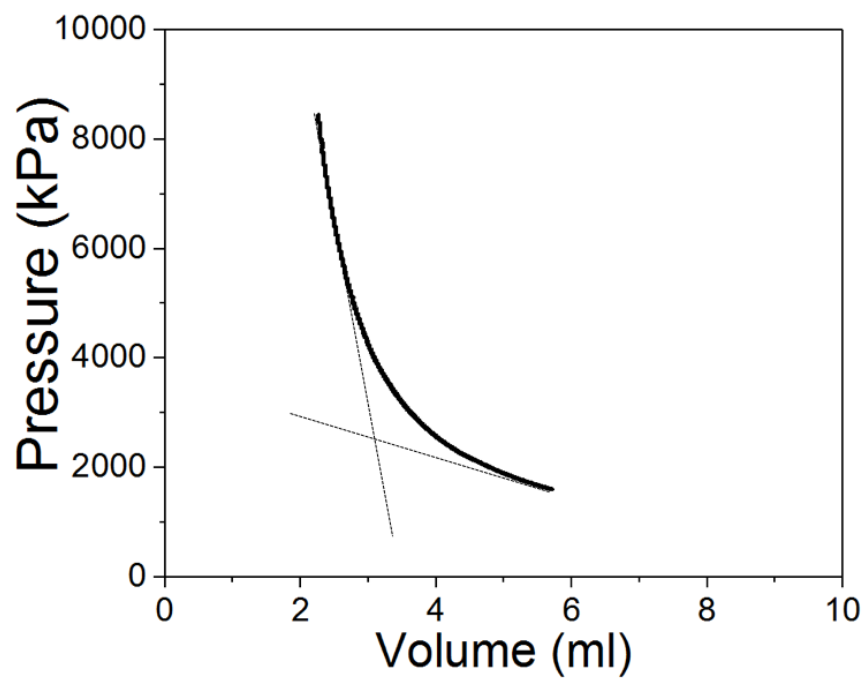
Figure 4.5 Experimentally obtained Pressure-Volume graph from the bubble point

measurement of decane-methane with 90:10 molar ratio at 21 ^{o}C (without porous media).

Figure 4.6 Experimentally obtained Pressure-Volume graph from the bubble point

measurement of decane-methane with a 90:10 molar ratio in the Niobrara sample at 21

°C.

CHAPTER 5

CONCLUSIONS AND FUTURE RESEARCH

Currently, there is a huge gap in the understanding of the storage and transport of hydrocarbons in shale reservoirs. When the dimensions of pores are comparable to the mean free path of the fluids molecules, their collisions with the wall of the pores cannot be neglected. At the nanoscale, in a confined porous system in shales and similar low-permeability rock, a phase be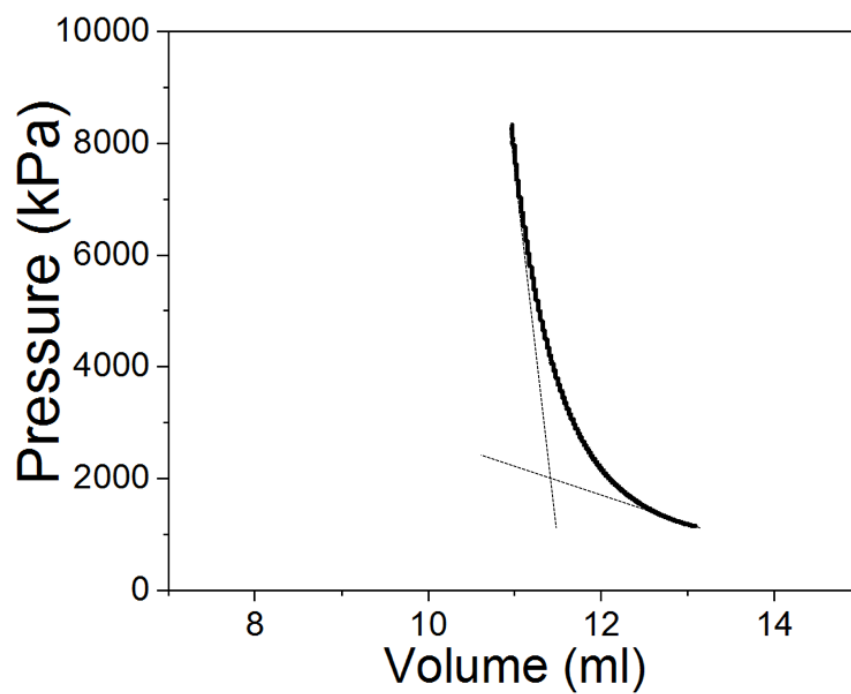havior of fluids depends not only fluid-fluid interactions, as in the bulk state, but also fluid-pore wall interactions. The pore surface area per unit volume increases as pore dimension decrease; therefore, the surface forces are not negligible at nanoscale. Due to these reasons, it has been hypothesized that hydrocarbons have different phase behaviors when they are in a confined system, and many theoretical approaches have been carried out to suggest this. However, there has been no direct experimental study to prove theses hypotheses. In this study, the phase behavior of hydrocarbons in nano-sized confinement systems was experimentally studied. Bubble points and boiling points of hydrocarbons in nano-sized porous media were measured to understand the phase behavior of confined fluids.

The direct measurements of bubble points for hydrocarbon mixtures (decane-methane and octane-methane) with a 90:10 mole ratio were undertaken in several nano-sized porous media. The nano-sized porous media included two synthesized siliceous

mesoporous materials having a pore size of about 4 nm (SBA-15 and SBA-16) and a Niobrara formation outcrop sample. For the purpose of pore size comparison, the bubble point of hydrocarbon mixtures in sand particles having micron-sized pores and in the bulk fluids (without porous media) were also measured. In addition, mesoporous monoliths with no macro pores were synthesized using a unique method developed for this study. The effect of only nano-sized pores on the bubble point were studied using the synthesized monoliths. BET measurements, pore size distribution curves, and TEM images were used to characterize the synthesized materials and, the results showed them having uniform nano-sized pores. Bubble points with micron-sized sand particles were close to those in the bulk fluids measurements (without porous media). However, the bubble points of hydrocarbons in nano-sized pores are lower than the values in the bulk fluids. Furthermore, the boiling point of decane in nano-sized porous media (monoliths) was found to be different than for pure decane using DSC and TGA. These measurements provide the evidence that the phase behavior of hydrocarbons may be suppressed in nano-sized porous media, such as found in shale reservoirs.

The correct estimation of fluid thermodynamic properties, including a bubble point, is essential to make better predictions of the amount of reserved oil and gas and the rates of recovery of them from shale reservoirs. A conventional PVT simulator, which calculates a bubble point, does not account for the effect of within-pores confinement because it is negligible in conventional reservoirs; however, there have been questions about the applicability of these measurements for shale reservoirs having nano-sized pores. This research provides evidence that the conventional simulator should be updated.

This research points to three new exciting areas of study to more thoroughly

understand a porous system. These areas of research are critical to being able to represent shale reservoirs in calculations designed to predict PVT properties for effective oil extraction from shales. First of all, the specific factors affecting the PVT properties of hydrocarbons need to be studied. Using the research presented in this dissertation on the effect of within-pores confinement on bubble points, the next step could be a study on the effect of pore morphologies, including pore size, pore structure, porosity, and wettability on the PVT properties of hydrocarbons. In materials having nano-sized pores, pore morphologies are important factors because they significantly affect the physical and chemical properties of their confined fluids. The second future research topic could be the effect of different compositions of porous materials on PVT properties. In this dissertation, only siliceous materials were studied. In addition to quartz (silica), shale reservoirs are composed of many different minerals, including plagioclase, calcite, dolomite, pyrite, and kaolinite. Depending on the particular composition of a shale reservoir, PVT properties will vary because of the different molecular interactions between the pore walls and fluids in the different minerals. The first two areas of research would lead to a better understanding of the factors affecting the PVT properties of hydrocarbons, and, thus, should be considered in new calculations for oil extraction from shale reservoirs. Studying the effect of these factors on permeability can complement research on understanding porous systems.

Taken together, the results of the theses research projects will (1) play a role in connecting the understanding of porous systems with building a new calculation standard for PVT properties of hydrocarbons in shale reservoirs; and (2) are necessary in order to efficiently and economically produce energy from shale reservoirs.

REFERENCES

(1)   *Key World Energy Statistics 2016*; 2016.

(2)   Hubbert, M. K. *Science (80-.)*. **1949**, *109* (2823), 103–109.

(3)   Pitakbunkate, T.; Balbuena, P. B.; Texas, A.; Moridis, G. J.; National, L. B. In *SPE Annual Technical Conference and Exhibition*; Society of Petroleum Engineers: Amsterdam, Netherlands, 2014.

(4)   Du, L.; Chu, L. In *SPE Canadian Unconventional Resources Conference*; Society of Petroleum Engineers: Calgary, Alberta, Canada, 2012.

(5)   *International Energy Outlook 2016*; 2016.

(6)   U.S. Energy Information Administration. *Drilling Productivity Report July 2017*; 2017.

(7)   Barrufet, M. A.; Wirawan, J. F. S.; Iglesias-Silva, G. A. *J. Chem. Eng. Data* **1995**, *40* (5), 1072–1075.

(8)   Firincioglu, T.; Llc, N.; Ozgen, C.; Ozkan, E. In *SPE Annual Technical Conference and Exhibition*; Society of Petroleum Engineers: New Orleans, Louisiana, USA, 2013.

(9)   Luo, S.; Nasrabadi, H.; Lutkenhaus, J. L. *Am. Inst. Chem. Eng.* **2016**, *62* (5), 1772–1780.

(10)   Didar, B. R.; Akkutlu, I. Y. In *SPE International Symposium on Oilfield Chemistry*; Society of Petroleum Engineers: Woodlands, Texas, USA, 2013.

(11)   Xiong, Y.; Winterfeld, P.; Wang, C.; Huang, Z.; Wu, Y.-S. In *SPE Annual Technical Conference and Exhibition*; Society of Petroleum Engineers: Houston, Texas, USA, 2015.

(12)   Teklu, T. W.; Alharthy, N.; Kazemi, H.; Yin, X.; Graves, R. M.; AlSumaiti, A. M. *SPE Reserv. Eval. Eng.* **2014**, *17* (3), 396–403.

(13)   Pitakbunkate, T.; Balbuena, P. B.; Moridis, G. J.; Blasingame, T. A. *Soc. Pet. Eng. J.* **2016**, *21* (2), 621–634.

(14)   Alharthy, N. S.; Nguyen, T. N.; Kazemi, H.; Teklu, T. W.; Graves, R. M. In *SPE*

Annual Technical Conference and Exhibition; Society of Petroleum Engineers: New Orleans, Louisiana, USA, 2013.

(15)   Tsukahara, T.; Maeda, T.; Hibara, A.; Mawatari, K.; Kitamori, T. *RSC Adv.* **2012**, *2* (8), 3184–3186.

(16)   Sanaei, A.; Jamili, A.; Callard, J. In *5th International conference on porous media and its applications in science and engineering (ICPM5)*; Kona, Hawaii, 2014.

(17)   Zarragoicoechea, G. J.; Kuz, V. A. *Phys. Rev. E* **2002**, *65* (2), 1–4.

(18)   Zarragoicoechea, G. J.; Kuz, V. A. *Fluid Phase Equilib.* **2004**, *220* (1), 7–9.

(19)   Dong, X.; Liu, H.; Hou, J.; Wu, K.; Chen, Z. *Ind. Eng. Chem. Res.* **2016**, *55* (3), 798–811.

(20)   Cho, H.; Bartl, M. H.; Deo, M. *Energy & Fuels* **2017**, *31* (4), 3436–3444.

(21)   Sigmund, P. M.; Dranchuk, P. M.; Morrow, N. R.; Purvis, R. A. *Soc. Pet. Eng. J.* **1973**, *13* (2), 93–104.

(22)   Gubbins, K. E.; Long, Y.; Sliwinska-Bartkowiak, M. *J. Chem. Thermodyn.* **2014**, *74*, 169–183.

(23)   Buzinov, S. N.; Peshkin, M. . *J. Eng. Phys.* **1976**, *31* (6), 1419–1423.

(24)   Pathak, M.; Velasco, R.; Panja, P. In *SPE Annual Technical Conference and Exhibition*; Society of Petroleum Engineers (SPE): San Antonio, Texas, USA, 2017.

(25)   Jarrahian, A.; Moghadasi, J.; Heidaryan, E. *J. Pet. Sci. Eng.* **2015**, *126*, 69–77.

(26)   Nojabaei, B.; Johns, R. T.; Chu, L. *Reserv. Eval. Eng.* **2013**, *16* (3), 281–289.

(27)   Loucks, R. G.; Reed, R. M.; Ruppel, S. C.; Jarvie, D. M. *J. Sediment. Res.* **2009**, *79* (12), 848–861.

(28)   Pitakbunkate, T.; Balbuena, P. B.; Moridis, G. J.; Blasingame, T. A. *Soc. Pet. Eng. J.* **2016**, *21* (2), 621–634.

(29)   Luo, S.; Lutkenhaus, J. L.; Nasrabadi, H. *J. Pet. Sci. Eng.*

(30)   Luo, S.; Lutkenhaus, J. L.; Nasrabadi, H. *Langmuir* **2016**, *32*, 11506–11513.

(31)   Teklu, T. W.; Alharthy, N.; Kazemi, H.; Yin, X.; Ramona, M. In *Unconventional Resources Technology Conference (URTeC)*; Unconventional Resources Technology Conference (URTeC): Denver, Colorado, USA, 2013.

(32)   Morishige, K.; Fujii, H.; Uga, M.; Kinukawa, D. *Langmuir* **1997**, *13* (13), 3494–

3498.

(33)   Kang, S. P.; Lee, J. W.; Ryu, H. J. *Fluid Phase Equilib.* **2008**, *274* (1–2), 68–72.

(34)   Devegowda, D.; Sapmanee, K.; Cavan, F.; Sigal, R. In *SPE Annual Technical Conference and Exhibition*; Society of Petroleum Engineers: San Antonio, Texas, USA, 2012.

(35)   Sanyal, M. K.; Datta, A.; Hazra, S. *Pure Appl. Chem.* **2002**, *74* (9), 1553–1570.

(36)   Edelstein, A. S.; Cammarata, R. . *Nanomaterials: synthesis, properties and applications*; CRC Press, 1998.

(37)   Rao, C. N. R.; Cheetham, A. K. *J. Mater. Chem.* **2001**, *11*, 2887–2894.

(38)   Neimark, A. V.; Sing, K. S. W.; Thommes, M. In *Handbook of Heterogeneous Catalysis*; 2008; pp 721–738.

(39)   Anovitz, L. M.; Cole, D. R. *Rev. Mineral. Geochemistry* **2015**, *80*, 61–164.

(40)   Zhao, D.; Huo, Q.; Feng, J.; Chmelka, B. F.; Stucky, G. D. *J. Chem. Soc.* **1998**, *120* (24), 6024–6036.

(41)   Maheshwari, H.; Roehling, J. D.; Turner, B. A.; Abdinor, J.; Tran-Roehling, T. B.; Deo, M. D.; Bartl, M. H.; Risbud, S. H.; van Benthem, K. *J. Mater. Sci.* **2016**, *51* (9), 4470–4480.

(42)   Srivastan, S.; Darwish, N. a.; Gasem, K. a. M.; Robinson, R. L. *J. Chem. Eng. Data* **1992**, *37* (4), 516–520.

(43)   Gevantman, L. H. *CRC Handb. Chem. Phys.* **2015**, 5–8.

(44)   Serrano, D. P.; Calleja, G.; Botas, J. a.; Gutierrez, F. J. *Ind. Eng. Chem. Res.* **2004**, *43* (22), 7010–7018.

(45)   Hsu, Y.; Hsu, Y.; Hsu, H.; Yang, C. *Chem. Mater.* **2007**, *19* (28), 1120–1126.

(46)   Zhao, D.; Feng, J.; Huo, Q.; Melosh, N.; Fredrickson, G.; Chmelka, B.; Stucky, G. *Science (80-.).* **1998**, *279* (5350), 548–552.

(47)   Sakamoto, Y.; Kaneda, M.; Terasaki, O.; Zhao, D. Y.; Kim, J. M.; Stucky, G.; Shin, H. J.; Ryoo, R. *Nature* **2000**, *408* (6811), 449–453.

(48)   Kim, T.; Ryoo, R.; Gierszal, K. P.; Jaroniec, M.; Solovyov, L. A.; Sakamoto, Y.; Terasaki, O. *J. Mater. Chem.* **2005**, *15* (15), 1560–1571.

(49)   Yuan, B.; Zhang, X. P.; Chung, C. Y.; Zhu, M. *Mater. Sci. Eng. A* **2006**, *438–440* (SPEC. ISS.), 585–588.

(50) Glover, P. *Petrophysics MSc Course Notes*; 2000.

(51) McCain, W. D. *The properties of petroleum fluids*; Petroleum Pub. Co., 1973.

(52) Kuila, U.; Prasad, M. *Geophys. Prospect.* **2013**, *61* (2), 341–362.

(53) Travalloni, L.; Castier, M.; Tavares, F. W.; Sandler, S. I. *Chem. Eng. Sci.* **2010**, *65* (10), 3088–3099.

(54) Topka, P.; Karban, J.; Soukup, K.; Jirátová, K.; Šolcová, O. *Chem. Eng. J.* **2011**, *168* (1), 433–440.

(55) Liu, J.; Chen, C.-F.; Tsao, C.-W.; Chang, C.-C.; Chu, C.-C.; DeVoe, D. L. *Anal. Chem.* **2009**, *81* (7), 2545–2554.

(56) Kendall, E. L.; Wienhold, E.; Rahmanian, O. D.; DeVoe, D. L. *Sensors Actuators B Chem.* **2014**, *202*, 866–872.

(57) Van Bommel, M. J.; De Haan, A. B. *J. Non. Cryst. Solids* **1995**, *186*, 78–82.

(58) Garcia-Gonzalez, C. A.; Camino-Rey, M. C.; Alnaief, M.; Zetzl, C.; Smirnova, I. *J. Supercrit. Fluids* **2012**, *66*, 297–306.

(59) Rogacki, G.; Wawrzyniak, P. *J. Non. Cryst. Solids* **1995**, *186*, 73–77.

(60) Yang, H.; Shi, Q.; Tian, B.; Xie, S.; Zhang, F.; Yan, Y.; Tu, B.; Zhao, D. *Chem. Mater.* **2003**, *15* (2), 536–541.

(61) Scherer, G. W.; Hareid, S.; Nilsen, E.; Einarsrud, M.-A. *J. Non. Cryst. Solids* **1996**, *204* (3), 228–234.

(62) Smith, D. M.; Scherer, G. W.; Anderson, J. M. *J. Non. Cryst. Solids* **1995**, *188* (3), 191–206.

(63) Scherer, G. W.; Smith, D. M. *J. Non. Cryst. Solids* **1995**, *189*, 197–211.

(64) Lin, C. L.; Pang, Y. S.; Chao, M. C.; Chen, B. C.; Lin, H. P.; Tang, C. Y.; Lin, C. Y. *J. Phys. Chem. Solids* **2008**, *69* (2–3), 415–419.

(65) Cao, C.; Liu, S.; Li, Z. *J. Chem. Inf. Comput. Sci.* **1999**, *39*, 1105–1111.

(66) Dake, L. P. *Fundamentals of reservoir engineering*; ELSEVIER, 1978.

(67) Kuila, U.; Prasad, M.; Derkowski, A.; McCarty, D. K. In *SPE Annual Technical Conference and Exhibition*; Society of Petroleum Engineers, Ed.; Society of Petroleum Engineers (SPE): San Antonio, Texas, USA, 2012.

(68) Sing, K. S. W.; Everett, D. H.; Haul, R. a. W.; Moscou, L.; Pierotti, R. a.; Rouquérol, J.; Siemieniewska, T. *Pure Appl. Chem.* **1985**, *57*, 603–619.

(69)   Rouquerol, J.; Rouquerol, F.; Llewellyn, P.; Maurin, G.; Sing, K. *Adsorption by Powders and Porous Solids: Principles, Methodology and Application*; Academic Press, 1999.